SU(3) Polyakov linear-σ model in magnetic fields: Thermodynamics, higher-order moments, chiral phase structure, and meson masses

Abdel Nasser Tawfik[*]

Egyptian Center for Theoretical Physics (ECTP), Modern University for Technology and Information (MTI), 11571 Cairo, Egypt
and World Laboratory for Cosmology And Particle Physics (WLCAPP), Cairo, Egypt

Niseem Magdy

World Laboratory for Cosmology And Particle Physics (WLCAPP), 11571 Cairo, Egypt
and Brookhaven National Laboratory (BNL) - Department of Physics, P.O. Box 5000, Upton, New York 11973-5000, USA

Effects of an external magnetic field on various properties of quantum chromodynamics (QCD) matter under extreme conditions of temperature and density (chemical potential) have been analyzed. To this end, we use SU(3) Polyakov linear-σ model and assume that the external magnetic field (eB) adds some restrictions to the quarks' energy due to the existence of free charges in the plasma phase. In doing this, we apply the Landau theory of quantization, which assumes that the cyclotron orbits of charged particles in a magnetic field should be quantized. This requires an additional temperature to drive the system through the chiral phase transition. Accordingly, the dependence of the critical temperature of chiral and confinement phase transitions on the magnetic field is characterized. Based on this, we have studied the thermal evolution of thermodynamic quantities (energy density and trace anomaly) and the first four higher-order moment of particle multiplicity. Having all these calculations, we have studied the effects of the magnetic field on the chiral phase transition. We found that both critical temperature T_c and critical chemical potential increase with increasing magnetic field, eB. Last but not least, the magnetic effects of the thermal evolution of four scalar and four pseudoscalar meson states are studied. We concluded that the meson masses decrease as the temperature increases up to T_c. Then, the vacuum effect becomes dominant and rapidly increases with the temperature T. At low T, the scalar meson masses normalized to the lowest Matsubara frequency rapidly decrease as T increases. Then, starting from T_c, we find that the thermal dependence almost vanishes. Furthermore, the meson masses increase with increasing magnetic field. This gives a characteristic phase diagram of T vs external magnetic field eB. At high T, we find that the masses of almost all meson states become temperature independent. It is worthwhile to highlight that the various meson states likely have different critical temperatures.

I. INTRODUCTION

It is believed that at high temperatures and densities there should be phase transition(s) between confined nuclear matter and the quark-gluon plasma (QGP), where quarks and gluons are no longer confined inside hadron bags [1]. Various theoretical studies have been devoted to tackle the possible change in properties of the strongly interacting matter, when the phase transition(s) between hadronic and partonic phases take place under the effect of an external magnetic field [2–7]. It is conjectured that the strongly interacting system (hadronic or partonic) can respond to the external magnetic field with magnetization M and magnetic susceptibility χ_M [8]. Both quantities characterize the magnetic properties of the system of interest. Thus, the effects of the external magnetic field on the chiral condensates should be reflected in the chiral phase transition [9]. Also, the effects on the deconfinement order parameter (Polyakov loop) which includes the confinement-deconfinement phase transition can be studied [9].

In an external magnetic field, the hadronic and partonic states are investigated in different models, such as the hadron resonance gas (HRG) model [10], and other effective models [11–19]. The Nambu–Jona-Lasinio (NJL) model [20–22], the chiral perturbation theory [23–25], the quark model [26], and certain limits of QCD [27] are also implemented. Furthermore, there are some studies devoted to the magnetic effects on the dynamical quark masses [28]. The chiral magnetic effect was studied in context of the Polyakov NJL (PNJL) model [29]. Lattice QCD calculations in an external magnetic field were reported recently [9,30–33]. The Polyakov linear-σ model (PLSM) was implemented to estimate the effects of the magnetic field on the system [7,34,35].

In the present work, we add some restrictions to the quarks energy due to the existence of free charges in the plasma phase. To this end, we apply the Landau theory (Landau quantization) [36], which quantizes of the cyclotron orbits of charged particles in magnetic fields. We notice that this proposed configuration requires an additional temperature to drive the system through the chiral phase transition. Accordingly, we find that the values of the chiral condensates increase with increasing the external magnetic field [5]. A few remarks are now in order. In many different calculations for the thermal behavior of the chiral condensates and the deconfinement order parameter (Polyakov loop) using PNJL or NJL [2–4], the external magnetic field was not constant.

[*]http://atawfik.net/

Also, the dependence of the critical temperatures of chiral and confinement phase transitions on the magnetic field was analyzed [37]. Almost the same study was conducted in PLSM [5–7]. All these studies lead to almost the same pattern: the critical temperature of the chiral phase transition increases with increasing external magnetic field. But, the critical temperature of the confinement phase transition behaves oppositely. The latter behavior agrees—to some extent—with the lattice QCD calculations [9]. In the present work, we study the effects of an external magnetic field on the phase transition and deduce the phase-diagram curve using SU(3) PLSM [38].

In light of this, we recall that the PLSM is widely implemented in different frameworks and for different purposes. The LSM was introduced by Gell-Mann and Levy in 1960 [39], a long time before QCD was known to be the theory of strong interaction. Many studies have been performed with LSM, such as $\mathcal{O}(4)$ LSM [39], $\mathcal{O}(4)$ LSM at finite temperature [40,41], and U(N_f)$_r$ × U(N_f)$_l$ LSM for $N_f = 2$, 3, or even 4 quark flavors [42–45]. In order to obtain reliable results, Polyakov-loop corrections have been added to LSM, in which information about the confining glue sector of the theory was included in the form of a Polyakov-loop potential. This potential is to be extracted from the pure Yang-Mills lattice simulations [46–49]. So far, many studies were devoted to investigating the phase diagram and the thermodynamics of PLSM at different Polyakov-loop forms with two [50,51] and three quark flavors [38,52,53]. Also, the magnetic field effect on the QCD phase transition and other system properties are investigated using PLSM [7,34,35].

The present paper is organized as follows. In Sec. II, we introduce details about SU(3) PLSM under the effects of an external magnetic field. Section III gives some features of the PLSM in an external magnetic field, such as the quark condensates, Polyakov loop, some thermal quantities, the phase transition(s), and scalar and pseudoscalar meson masses under the magnetic field effect. In Sec. IV, the final conclusions and outlook are presented.

II. APPROACH

The Lagrangian of LSM with $N_f = 2 + 1$ quark flavors and $N_c = 3$ color degrees of freedom, where the quarks couple to the Polyakov-loop dynamics, was introduced in Refs. [38,52,53],

$$\mathcal{L} = \mathcal{L}_{\text{chiral}} - \mathcal{U}(\phi,\phi^*,T), \tag{1}$$

where the chiral part of the Lagrangian $\mathcal{L}_{\text{chiral}} = \mathcal{L}_q + \mathcal{L}_m$ has SU(3)$_L$ × SU(3)$_R$ symmetry [54,55]. The Lagrangian with $N_f = 2 + 1$ consists of two parts. The first part represents fermions, Eq. (2), with a flavor-blind Yukawa coupling g of the quarks. The coupling between the effective gluon field and quarks, and between the magnetic field B and the quarks, is implemented through the covariant derivative [7]

$$\mathcal{L}_q = \sum_f \overline{\psi}_f (i\gamma^\mu D_\mu - g T_a(\sigma_a + i\gamma_5 \pi_a))\psi_f, \tag{2}$$

where the summation $\sum_f$ runs over the three flavors, $f = 1, 2, 3$ for u, d, and s quarks, respectively, and T_a are the Gell-Man matrices. The flavor-blind Yukawa coupling, g, should

couple the quarks to the mesons [56]. The coupling of the quarks to the Euclidean gauge field, A_μ, was discussed in Refs. [46,47]. For the Abelian gauge field, the influence of the external magnetic field, A_μ^M, [34] is given by the covariant derivative [7],

$$D_\mu = \partial_\mu - i A_\mu - i Q A_\mu^{EM}, \tag{3}$$

where $A_\mu = g A_\mu^a \lambda^a/2$ and $A_\mu^{EM} = (0, Bx, 0, 0)$, and Q is a matrix defined by the quark electric charges $Q = \text{diag}(q_u, q_d, q_s)$ for up, down, and strange quarks, respectively. The interaction of charged pions $\pi^\pm = (\pi_1 \pm i\pi_2)/\sqrt{2}$ with the magnetic field is included by $D_\mu = \partial_\mu - i e A_\mu^M$, where e is the electric charge [7].

The second part of chiral Lagrangian stands for the the mesonic contribution, Eq. (4),

$$\begin{aligned}\mathcal{L}_m = {}&\text{Tr}(\partial_\mu \Phi^\dagger \partial^\mu \Phi - m^2 \Phi^\dagger \Phi) - \lambda_1[\text{Tr}(\Phi^\dagger \Phi)]^2 \\ &- \lambda_2 \text{Tr}(\Phi^\dagger \Phi)^2 + c[\text{Det}(\Phi) + \text{Det}(\Phi^\dagger)] \\ &+ \text{Tr}[H(\Phi + \Phi^\dagger)].\end{aligned} \tag{4}$$

In Eq. (4), Φ is a complex 3×3 matrix, which depends on the σ_a and π_a [55], where γ^μ are the chiral spinors, σ_a are the scalar mesons and π_a are the pseudoscalar mesons.

The second term in Eq. (1), $\mathcal{U}(\phi,\phi^*,T)$, represents the Polyakov-loop effective potential [46], which is expressed by using the dynamics of the thermal expectation value of a color traced Wilson loop in the temporal direction $\Phi(\vec{x}) = \langle \mathcal{P}(\vec{x}) \rangle / N_c$. Then, the Polyakov-loop potential and its conjugate read $\phi = (\text{Tr}_c \mathcal{P})/N_c$ and $\phi^* = (\text{Tr}_c \mathcal{P}^\dagger)/N_c$, respectively. $\mathcal{P}$, which stands for the Polyakov loop, can be represented by a matrix in the color space [46]

$$\mathcal{P}(\vec{x}) = \mathcal{P} \exp\left[i \int_0^\beta d\tau A_4(\vec{x},\tau)\right], \tag{5}$$

where $\beta = 1/T$ is the inverse temperature and $A_4 = iA^0$ is the Polyakov gauge [46,47]. The Polyakov-loop matrix can be given as a diagonal representation [57].

In the PLSM Lagrangian, Eq. (1), the coupling between the Polyakov loop and the quarks is given by the covariant derivative of $D_\mu = \partial_\mu - iA_\mu$ [53]. It is apparent that the PLSM Lagrangian is invariant under the chiral flavor group. This is similar to the original QCD Lagrangian [58–60]. In order to reproduce the thermodynamic behavior of the Polyakov loop for pure gauge, we use a temperature-dependent potential $U(\phi,\phi^*,T)$. This should agree with the lattice QCD simulations and have Z(3) center symmetry like the pure gauge QCD Lagrangian [59,61]. In the case of vanishing chemical potential, then $\phi = \phi^*$ and the Polyakov loop is considered an order parameter for the deconfinement phase transition [59,61]. In the present work, we use $U(\phi,\phi^*,T)$, a Landau-Ginzburg type potential, as a polynomial expansion in ϕ and ϕ^* [58–61]:

$$\frac{\mathcal{U}(\phi,\phi^*,T)}{T^4} = -\frac{b_2(T)}{2}\phi\,\phi^* - \frac{b_3}{6}(\phi^3 + \phi^{*3}) + \frac{b_4}{4}(\phi\,\phi^*)^2, \tag{6}$$

where ϕ and ϕ^* were introduced previously and $b_2(T) = a_0 + a_1(T_0/T) + a_2(T_0/T)^2 + a_3(T_0/T)^3$, where constants are $a_0 = 6.75$, $a_1 = -1.95$, $a_2 = 2.625$, $a_3 = -7.44$, $b_3 = 0.75$, and $b_4 = 7.5$.

In Eq. (6), the Vandermonde Jacobian contribution, $\kappa \ln[J(\phi,\phi^*)]$, was ignored due the small value of κ. In principle, the Vandermonde term comes from the change of variables from vector potential to ϕ in the path integral and should guarantee a reasonable behavior of the mean field approximation [62]; i.e., it was suggested to solve the problem that the normalized Polyakov loop becomes greater than 1 at very high temperatures:

$$J[\phi,\phi^*] = \frac{27}{24\pi^2}[1 - 6\phi\,\phi^* + 4(\phi^3 + \phi^{*3}) - 3(\phi\,\phi^*)^2],$$

where $J(\phi,\phi^*)$ is the Vandermonde determinant, which is not explicitly space-time dependent. The dimensionless parameter κ would be dependent on the temperature and the chemical potential. Therefore, κ should be estimated phenomenologically.

In order to reproduce the pure gauge QCD thermodynamics and the behavior of the Polyakov loop as a function of temperature, we use the parameters listed above in this section [59]. In calculating the grand potential, we use the mean field approximation [38],

$$\Omega(T,\mu) = U(\sigma_x,\sigma_y) + \mathcal{U}(\phi,\phi^*,T) + \Omega_{\bar{\psi}\psi}(T;\phi,\phi^*,B). \quad (7)$$

The purely mesonic potential is given as

$$U(\sigma_x,\sigma_y) = \frac{m^2}{2}\big(\sigma_x^2 + \sigma_y^2\big) - h_x\sigma_x - h_y\sigma_y - \frac{c}{2\sqrt{2}}\sigma_x^2\sigma_y$$
$$+ \frac{\lambda_1}{2}\sigma_x^2\sigma_y^2 + \frac{1}{8}(2\lambda_1 + \lambda_2)\sigma_x^4 + \frac{1}{4}(\lambda_1 + \lambda_2)\sigma_y^4, \quad (8)$$

where m^2, h_x, h_y, λ_1, λ_2, and c are the model fixed parameters [55]. The quarks and antiquark contribution to the medium potential was introduced in Ref. [63], and based on Landau quantization and magnetic catalysis concepts, Appendix A, we get

$$\Omega_{\bar{\psi}\psi}(T,\mu_f,eB) = -2\sum_f \frac{|q_f|BT}{2\pi}\sum_{\nu=0}^{\infty}\int\frac{dp}{2\pi}(2 - 1\delta_{0\nu})$$
$$\times\Big\{\ln\Big[1 + 3(\phi + \phi^*e^{-\frac{(E_f-\mu_f)}{T}})$$
$$\times e^{-\frac{(E_f-\mu_f)}{T}} + e^{-3\frac{(E_f-\mu_f)}{T}}\Big]$$
$$+ \ln\Big[1 + 3(\phi^* + \phi e^{-\frac{(E_f+\mu_f)}{T}})$$
$$\times e^{-\frac{(E_f+\mu_f)}{T}} + e^{-3\frac{(E_f+\mu_f)}{T}}\Big]\Big\}. \quad (9)$$

It is worthwhile to highlight that the chemical potential used everywhere in the manuscript is the quark one, μ_f, with f being the quark flavor. The different variables are elaborated in Appendix A. The potential at vanishing eB reads

$$\Omega_{\bar{q}q}(T,\mu_f) = -2\,T\sum_{f=l,s}\int_0^{\infty}\frac{d^3\vec{p}}{(2\pi)^3}$$
$$\times\{\ln[1 + 3(\phi + \phi^*e^{-(E_f-\mu_f)/T})$$
$$\times e^{-(E_f-\mu_f)/T} + e^{-3(E_f-\mu)/T}]$$
$$+ \ln[1 + 3(\phi^* + \phi e^{-(E_f+\mu_f)/T})$$
$$\times e^{-(E_f+\mu_f)/T} + e^{-3(E_f+\mu)/T}]\}. \quad (10)$$

This is the system free of Landau quantization.

The Landau theory quantizes the cyclotron orbits of charged particles in a magnetic field. For small magnetic fields, the number of occupied Landau levels (LLs) is large and the quantization effects are washed out, while for large magnetic fields the Landau levels are less occupied and the chiral symmetry restoration occurs for smaller values of the chemical potential.

According to Eqs. (9) and (10), Eq. (7) get an additional term,

$$\Omega(T,\mu_f,eB) = U(\sigma_x,\sigma_y) + \mathcal{U}(\phi,\phi^*,T)$$
$$+ \Omega_{\bar{\psi}\psi}(T,\mu_f;\phi,\phi^*,eB)$$
$$+ \delta_{0,eB}\Omega_{\bar{\psi}\psi}(T,\mu_f;\phi,\phi^*), \quad (11)$$

where $\Omega_{\bar{\psi}\psi}(T,\mu_f;\phi,\phi^*)$ represents the potential term at vanishing magnetic field, and $\delta_{0,eB}$ switches between the two systems: one at vanishing and one at finite magnetic field.

We notice that the sum in Eqs. (6), (9), and (8) give the thermodynamic potential density as in Eq. (7). By using the minimization condition, Appendix B, we can evaluate the parameters. Having the thermodynamic potential, Eq. (7), we can determine all thermal quantities including the higher-order moments of particle multiplicity, and then map out the chiral phase diagram [38]. The meson masses are defined by the second derivative with respect to the corresponding fields of the grand potential, Eq. (7), evaluated at its minimum.

III. RESULTS

The results of the chiral condensates σ_x and σ_y, Sec. III A, the thermodynamic quantities, Sec. III B, the non-normalized and normalized higher-order moment of particle multiplicity, Secs. III C and III C 2, respectively, the chiral phase-transition, Sec. III D and finally the meson masses, Sec. III E, are introduced as follows.

A. Phase transition: Quark condensates and order parameters

The thermal evolution of the chiral condensates, σ_x and σ_y, and the Polyakov order parameters, ϕ and ϕ^*, is calculated from Eq. (7) at finite chemical potential and finite magnetic field using the minimization conditions given in Eq. (B1). The dependence of the minimization condition on the four parameters—temperature T, chemical potential μ, magnetic field B and minimization parameter with respect to it—is analyzed.

In left-hand panel (a) of Fig. 1, the normalized chiral condensates, σ_x and σ_y, are given as functions of temperature at
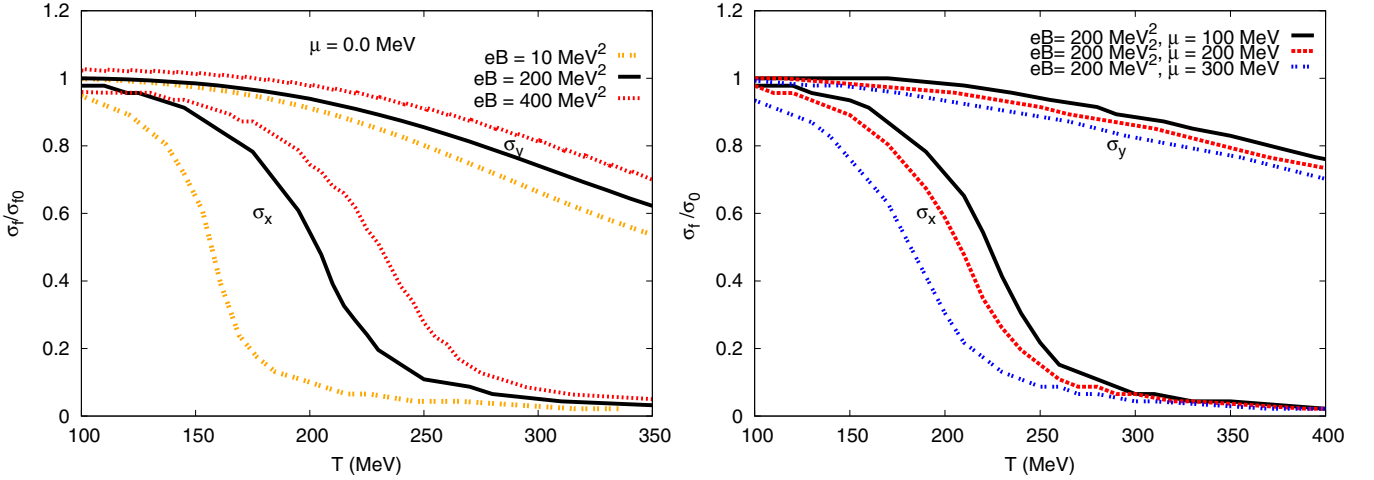
FIG. 1. (Color online) Left-hand panel (a): the normalized chiral-condensates, σ_x (lower curves) and σ_y (upper curves), are given as function of temperature at vanishing chemical potential and different magnetic field values, $eB = 10\,\text{MeV}^2$ (double-dotted curve), $200\,\text{MeV}^2$ (solid curve), and $400\,\text{MeV}^2$ (dotted curve). Right-hand panel (b): the same as in left-hand panel but at a constant magnetic field $eB = 200\,\text{MeV}^2$ and different quark chemical potentials $\mu = 100\,\text{MeV}$ (solid curve), $200\,\text{MeV}$ (dotted curve), and $300\,\text{MeV}$ (double-dotted curve).

vanishing chemical potential and different magnetic values, $eB = 10\,\text{MeV}^2$ (double-dotted curve), $200\,\text{MeV}^2$ (solid curve), and $400\,\text{MeV}^2$ (dotted curve). We notice that both condensates increase with increasing magnetic field, eB. This dependence seems to explain the increase in the chiral critical temperature T_c with the magnetic field. This in turn agrees with various studies using PLSM and PNJL [2–7]. The condensates become moderated (smoother) with increasing magnetic field.

The right-hand panel (b) of Fig. 1 shows the chiral condensates, σ_x and σ_y, as function of temperature at constant magnetic field $eB = 200\,\text{MeV}^2$, and finite chemical potentials $\mu = 100\,\text{MeV}$ (solid curve), $200\,\text{MeV}$ (dotted curve), and $300\,\text{MeV}$ (double-dotted curve). Both condensates decrease with increasing the chemical potentials. This dependence gives a signature for the decreasing behavior of the chiral critical temperature T_c with increasing the chemical potential, which obviously agrees with our previous calculations [38]. The condensates become rowdy (sharper) with increasing chemical potential.

The left-hand panel (a) of Fig. 2 shows the Polyakov-loop field and it is conjugation, ϕ (upper curves) and ϕ^* (lower curves), as function of temperature at a vanishing chemical potential and different magnetic field values, $eB = 0.01\,\text{GeV}^2$ (double-dotted curve), $0.2\,\text{GeV}^2$ (solid curve), and $0.4\,\text{GeV}^2$ (dotted curve). Both fields decrease with increasing magnetic field. This behavior explains the dependence of the confinement critical temperature on the magnetic field. At vanishing chemical potential, $\phi = \phi^*$. Both Polyakov-loop fields become smoother with increasing magnetic field.

The right-hand panel (b) shows the same as in the left-hand panel but at a constant magnetic field $eB = 0.2\,\text{GeV}^2$ and
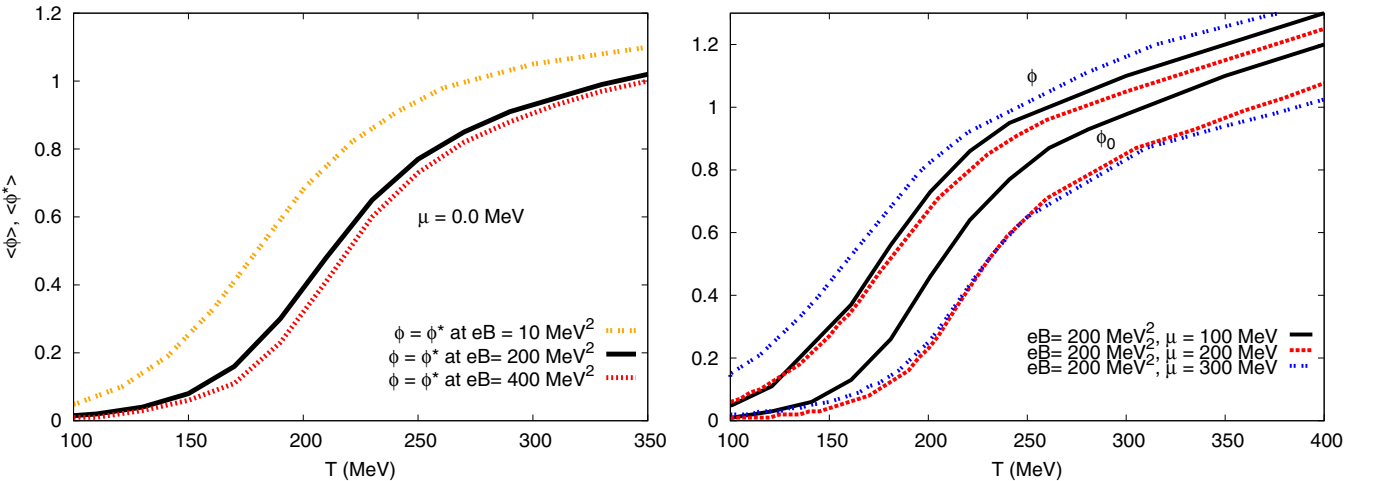

FIG. 2. (Color online) Left-hand panel (a): the Polyakov-loop field and its conjugation, ϕ and ϕ^*, are given as function of temperature at a vanishing constant chemical potential and different magnetic field values, $eB = 10\,\text{MeV}^2$ (double-dotted curve), $0.2\,\text{GeV}^2$ (solid curve), and $400\,\text{MeV}^2$ (dotted curve). Right-hand panel (b): the same as in the left-hand panel but at a constant magnetic field $eB = 0.2\,\text{GeV}^2$ and different quark chemical potential values, $\mu = 0.1\,\text{GeV}$ (solid curve), $0.2\,\text{GeV}$ (dashed curve) and $0.3\,\text{GeV}$ (double-dotted curve).
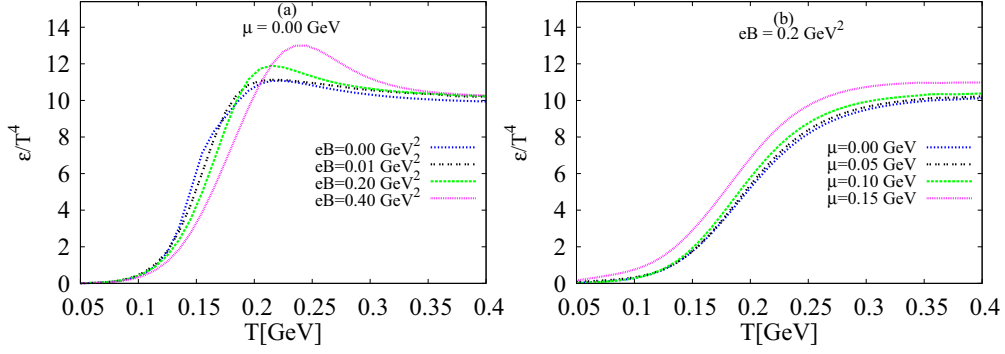
FIG. 3. (Color online) Left-hand panel (a): the normalized energy density ϵ/T^4 is given as function of temperature at a vanishing chemical potential and different magnetic fields: without magnetic field (solid curve) [38], $eB = 0.01$ GeV^2 (long-dashed curve), $eB = 0.2$ GeV^2 (dashed curve), and $eB = 0.4$ GeV^2 (double-dotted curve). The right-hand panel (b) shows the same as in the left-hand panel but at a constant magnetic field $eB = 0.2$ GeV^2 and different chemical potential values, $\mu = 0.1$ GeV (long-dashed curve), 0.2 GeV (dash-dotted curve), and 0.3 GeV (double-dotted curve). The upper curves represent results from Eq. (9) plus Eq. (10), while lower curves are based on thermodynamic derivatives from the thermal potential, Eq. (9).

different quark chemical potential values, $\mu = 0.1$ GeV (solid curve), 0.2 GeV (dashed curve), and 0.3 GeV (double-dotted curve). We find that ϕ increases with increasing chemical potential values but ϕ^* decreases. This behavior seems to agree with our previous calculations [38]. At finite chemical potential, $\phi > \phi^*$.

We conclude that the Polyakov-loop fields ϕ and ϕ^* increase with T; see Fig. 2. At vanishing μ, both ϕ and ϕ^* decrease with increasing eB. At finite μ, we find that ϕ increases, while ϕ^* decreases with eB.

B. Thermodynamic quantities

In this section, we introduce some thermal quantities such as energy density and trace anomaly. As we discussed in Ref. [38], the purely mesonic potential, Eq. (8), goes to infinity at very low temperature and entirely vanishes at high temperature. From this numerical estimation, we concluded that this part of potential is only effective at very low temperatures. Its dependence on the external magnetic field has been checked, and it was found that finite eB yields a very tiny contribution to this potential part. As the present study is performed at temperatures around the critical one, this potential part can be removed from the effective potentials given in Eq. (7). In Eq. (8), the chiral condensates, σ's, are

small at finite temperature; see Fig. 1. Therefore, much smaller values are expected for their higher orders and multiples. The opposite situation is likely at very small temperatures.

1. Energy density

The energy density ϵ/T^4 at finite quark chemical potential μ_f can be obtained as

$$\epsilon(T,\mu_f,eB) = -\frac{\partial}{\partial(1/T)} \ln Z(T,\mu_f,eB). \qquad (12)$$

In Sec. III A we estimated the parameters: the two chiral condensates σ_x and σ_y and the two order parameters of the Polyakov loop and its conjugation, ϕ and ϕ^*, respectively. Thus, we can substitute all these into Eq. (12).

The left-hand panel (a) of Fig. 3 presents the normalized energy density ϵ/T^4 as a function of temperature at vanishing chemical potential. In calculating the results, Eqs. (9) and (10) are implemented as given in Eq. (11). The general temperature dependence is not absent. Also, we notice that ϵ/T^4 is sensitive to the change in eB [63]. Increasing eB seems to increase the critical temperature at which the system undergoes phase transition. As the chiral condensates become smoother with increasing eB, the thermodynamic quantities, such as energy
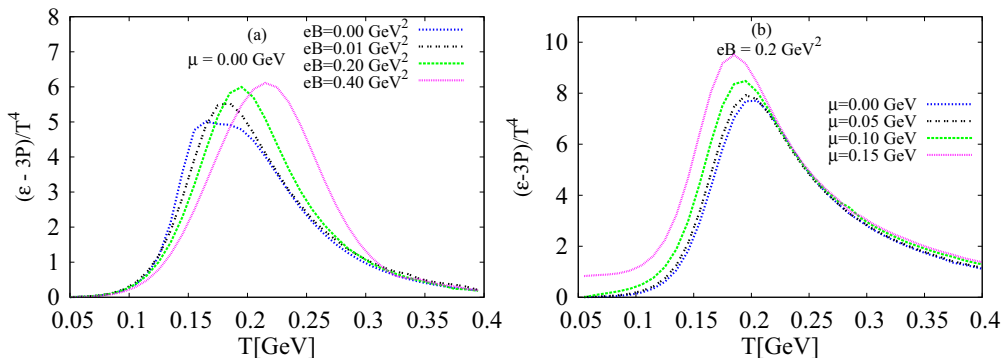

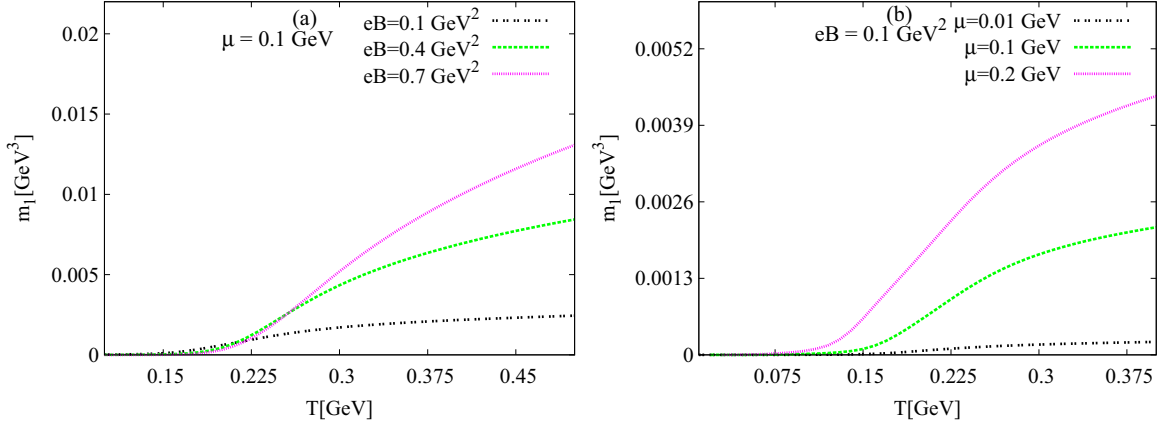FIG. 4. (Color online) The same as in Fig. 3 but for the the trace anomaly $(\epsilon - 3p)/T^4$.

FIG. 5. (Color online) Left-hand panel (a): the non-normalized quark number density, m_1, is given as function of temperature at a constant chemical potential $\mu = 0.1$ GeV and different values of the magnetic field, $eB = 0.1$ GeV^2 (double-dotted curve), 0.4 GeV^2 (dashed curve), and 0.7 GeV^2 (dotted curve). The right-hand panel (b) shows the same as the left-hand panel but at a constant magnetic field $eB = 0.1$ GeV^2 and different chemical potentials, $\mu = 0.01$ GeV (double-dotted curve), 0.1 GeV (dashed curve), and 0.2 GeV (dotted curve).

density, behave accordingly, i.e., the phase transition becomes smoother as well.

The right-hand panel (b) shows ϵ/T^4 as function of temperature at a constant magnetic field $eB = 0.2$ GeV^2 and varying quark chemical potentials $\mu = 0.1$ GeV (long-dashed curve), 0.2 GeV (dash-dotted curve), and 0.3 GeV (double-dotted curve). The solid curve represents the results in the absence of an external magnetic field but at $\mu = 0.1$ GeV. We note that ϵ/T^4 is not as sensitive to the change in μ [38] as to the external magnetic field. Despite the lack of chemical potential dependency, which can be understood due to the large magnetic field applied, it is believed to have an effect contrary to that of the chemical potential. To this indirect dependency of μ and eB, we shall devote a separate work. Again, it seems that increasing μ_f decreases T_c.

2. Trace anomaly

At finite quark chemical potential, the trace anomaly known as interaction measure reads

$$\frac{\epsilon(T,\mu_f,eB) - 3p(T,\mu_f,eB)}{T^4} = T\frac{\partial}{\partial T}\frac{p(T,\mu_f,eB)}{T^4}. \quad (13)$$

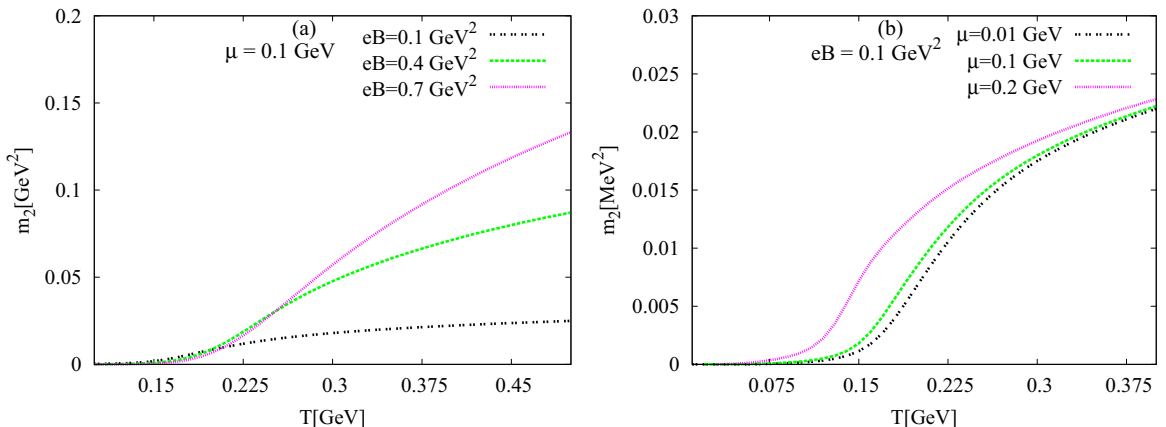In Fig. 4, we notice that the normalized trace anomaly under the effect of an external magnetic field becomes smaller than the corresponding quantity in absence of a magnetic field [38] at high temperature. This can be explained due the restrictions added to the quark energy by the Landau quantization through the magnetic field. We find that increasing eB increases the critical temperature. This behavior can be understood because of the dependence of the chiral condensates, Fig. 1, and the Polyakov-loop potential, Fig. 2, on eB.

In the left-hand panel (a), the trace anomaly $(\epsilon - 3p)/T^4$, is given as function of temperature T at vanishing chemical potential but different values of the magnetic fields: vanishing [38] (solid curve), $eB = 0.01$ GeV^2 (long-dashed curve), $eB = 0.2$ GeV^2 (dash-dotted curve), and $eB = 0.4$ GeV^2 (double-dotted curve). We notice that the trace anomaly increases with T until the chiral symmetry is restored. Then, increasing T reduces the normalized trace anomaly. The peak represents the critical temperature T_c corresponding to a certain magnetic field. We find that T_c increases with increasing eB.

The right-hand panel (b) of Fig. 4 shows the same as in the left-hand panel but at a constant magnetic field $eB = 0.2$ GeV^2

FIG. 6. (Color online) The same as in Fig. 5 but for quark number susceptibility m_2.
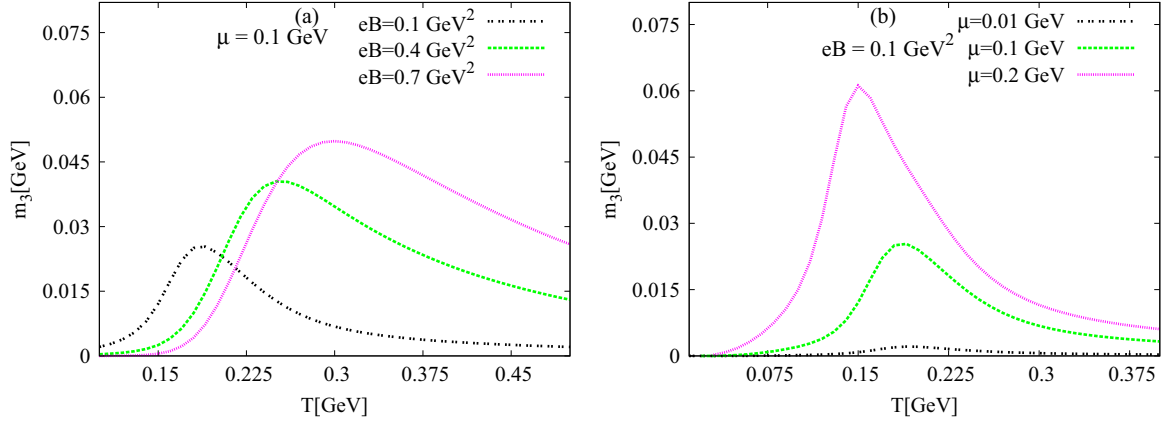
FIG. 7. (Color online) The same as in Fig. 5 but for the third-order moment of quark number density m_3.

and different chemical potentials $\mu = 0.0$ GeV (solid curve), 0.1 GeV (long-dashed curve), 200 MeV (dash-dotted curve), and 300 GeV (double-dotted curve). The trace anomaly increases with T until the chiral symmetry is fully restored. The peaks are positioned at T_c of the certain value for chemical potential. Here, we find that T_c decreases with increasing μ. The sensitivity to μ is not as strong as to eB. This might be interpreted that the high magnetic field applied seems to contradict the effects of the chemical potential. In other words, if the magnetic field adds energy to the system, the chemical potential requires energy in order to produce new particles. We notice that the dependence on the quark chemical potential is more obvious than that shown in Fig. 3.

3. Magnetic catalysis effect

In Appendix A, we discuss the magnetic catalysis, Eq. (A6), and the so-called dimension reduction concepts, Eq. (A6). Due to the effects of the magnetic field, the latter would mean modifying the sum over the three-dimensional momentum space to a one-dimensional one. According to Ref. [38], the effect of this reduction reduces also the value of the quantity by almost two-thirds from the expected value. This would explain the difference between results at vanishing and at finite eB, left-hand panels (a) of Figs. 3 and 4, for instance. In the present work, we distinguish between two types of systems. In

the first one, the Landau quantization should be implemented, i.e., taking into account the magnetic effects, while in the other system the external magnetic field is not taken into consideration, i.e., there is no magnetic contribution to the thermal system.

C. Higher-order moment of particle multiplicity

The higher-order moment of the particle multiplicity is defined [38,65] as

$$m_i = \frac{\partial^i}{\partial \mu^i} \frac{p(T,\mu,B)}{T^4}, \tag{14}$$

where the pressure $p(T,\mu,B) = -T \, \partial \ln \mathcal{Z}(T,\mu,B)/\partial V$ is related to the partition function, which in turn is related to the potential, $\ln \mathcal{Z}(T,\mu,B) = -V \, \Omega(T,\mu,B)/T$.

In this section, we introduce the first four non-normalized moments of the particle multiplicity calculated in PLSM under the effects of an external magnetic field. The thermal evolution is studied at a constant chemical potential but different magnetic fields and also at a constant magnetic field but different chemical potentials. Doing this, it is possible to map out the chiral phase diagram, for which we determine the irregular behavior in the higher-order moments as a function of T and μ.
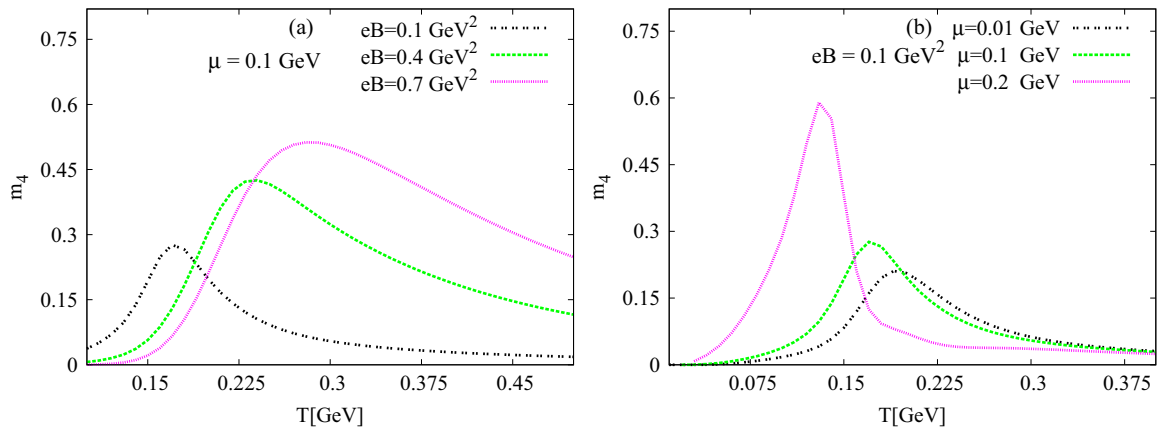
FIG. 8. (Color online) The same as in Fig. 5 but for the fourth-order moment of quark number density m_4.
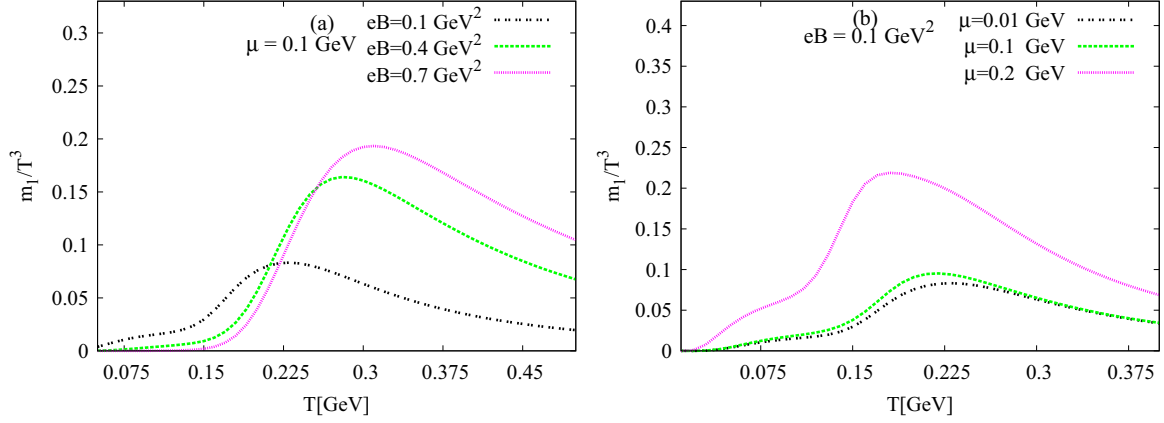
FIG. 9. (Color online) Left-hand panel (a): the dimensionless quark number density m_1/T^3 is given as a function of temperature at constant chemical potential $\mu = 0.1$ GeV and different magnetic fields, $eB = 0.1$ GeV^2 (double-dotted curve), $eB = 0.4$ GeV^2 (dashed curve), and $eB = 0.7$ GeV^2 (dotted curve). The right-hand panel (b) shows the same as in the left-hand panel but at a constant magnetic field $eB = 0.1$ GeV^2 and different chemical potential values, $\mu = 0.01$ GeV (double-dotted curve), $\mu = 0.1$ GeV (dashed curve), and $\mu = 0.2$ GeV (dotted curve).

1. Non-normalized higher-order moments

Here, we introduce the non-normalized higher-order moments of the particle multiplicity [38]. The left-hand panels (a) of Figs. 5, 6, 7, and 8 show the first four non-normalized moments of the quark distributions. These quantities are given as functions of temperature at a constant chemical potential $\mu = 0.1$ GeV and different magnetic fields $eB = 0.1$ GeV^2 (double-dotted curve), 0.4 GeV^2 (dashed curve), and 0.7 GeV^2 (dotted curve). We find that increasing temperature rapidly increases the four moments. Furthermore, the thermal dependence is obviously enhanced when moving from lower to higher orders. The values of the moment are increasing as we increase the magnetic field. The fluctuation in the third- and fourth-order moments reflect the increase of the critical temperature T_c with increasing magnetic field. The critical temperature can, for instance, be defined where the peaks are positioned.

The right-hand panels (b) of Figs. 5, 6, 7, and 8 present the same as in the left-hand panels but at a constant magnetic field $eB = 0.1$ GeV^2 and different chemical potentials, $\mu = 0.01$ GeV (double-dotted curve), 0.1 GeV (dashed curve), and 0.2 GeV (dotted curve). It is apparent that increasing

temperature rapidly increases the four moments of quark number density. Furthermore, the thermal dependence is obviously enhanced when moving from lower to higher orders. The values of the moments are increasing as we increase the chemical potential. But the critical temperature T_c decreases with μ. The peaks are positioned at the critical temperature.

2. Normalized higher-order moments

The statistical normalization of the higher-order moments requires a scaling of the non-normalized quantities, Sec. III C 1, with respect to the standard deviation σ, which is related to the susceptibility χ or the fluctuations [64,65] in the particle multiplicity. It is conjectured that the dynamical phenomena could be indicated by large fluctuations in these dimensionless moments and, therefore, the chiral phase-transition can be mapped out [64]. Due to the sophisticated derivations, we restrict the discussion here to dimensionless higher-order moments [38]. This can be done when the normalization is done with respect to the temperature or chemical potential.

The higher-order moments of the particle multiplicity normalized with respect to temperature are studied in dependence
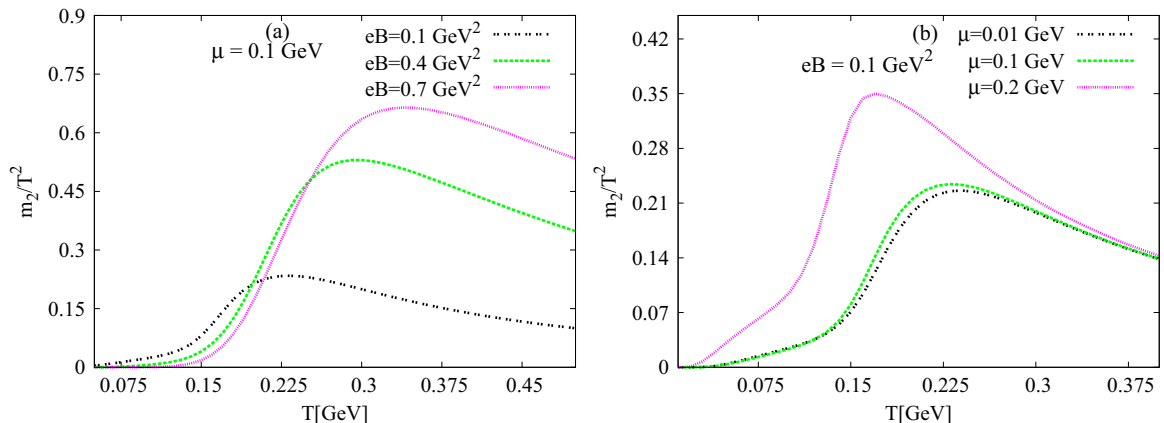

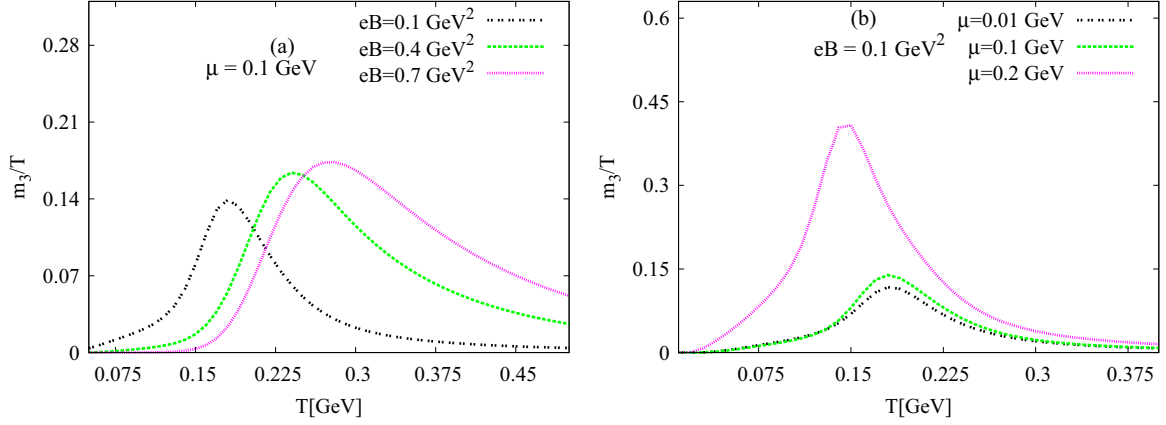FIG. 10. (Color online) The same as in Fig. 9 but for the dimensionless quark number susceptibility m_2/T^2.

FIG. 11. (Color online) The same as in Fig. 9 but for the dimensionless third-order moment of the quark number density m_3/T.

on the temperature at a constant chemical potential and different magnetic fields. Also they are studied at different chemical potentials and a constant magnetic field. The corresponding expressions were deduced in Ref. [38].

In the left-hand panels (a) of Figs. 9, 10, and 11 the first three normalized moments are given as functions of temperature at a constant chemical potential $\mu = 0.1$ GeV and different magnetic fields, $eB = 0.1$ GeV^2 (double-dotted curve), 0.4 GeV^2 (dashed curve), and 0.7 GeV^2 (dotted curve). We find that the values of the moments are increasing as the magnetic field increases. The fluctuations in the normalized moments would define the dependence of the critical temperature T_c on the magnetic field.

The right-hand panels (b) of Figs. 9, 10, and 11 present the first three normalized moments as function of temperature but at a constant magnetic field $eB = 0.1$ GeV^2 and different chemical potentials, $\mu = 0.01$ GeV (double-dotted curve), 0.1 GeV (dashed curve), and 0.2 GeV (dotted curve). We notice that the moments of quark multiplicity increase with the chemical potentialsthat the peaks at corresponding critical temperatures can be used to map out the chiral phase-diagrams, T vs eB and T vs μ.

D. Chiral phase transition

Now we can study the effects of the magnetic field on the chiral phase transition. In a previous work [38], we introduced and summarized different methods to calculate the critical temperature and chemical potential μ_c by using the fluctuations in the normalized higher-order moments of the quark multiplicity or by using the order parameters. The latter is implemented in the present work. The PLSM has two order parameters. The first one presents the chiral phase transition. This is related to strange and nonstrange chiral condensates, σ_x and σ_y. The second one gives hints for the confinement-deconfinement phase transition and the Polyakov-loop fields ϕ and ϕ^*. Therefore, for the models having Polyakov-loop potential, we can follow a procedure as follows. We start with a constant value of the magnetic field. By using strange and nonstrange chiral condensates, a dimensionless quantity reflecting the difference between the nonstrange and strange condensates $\Delta_{q,s}(T)$ as a function of temperature at fixed

chemical potentials will be implemented. This procedure gives *one point* in the T-μ chart, at which the chiral phase transition takes place. At the same chemical potential as in the previous step, we deduce the other order parameter related to the Polyakov-loop fields as a function of temperature. These calculations give another point (*in T and μ chart*), at which the deconfinement phase transition takes place. By varying the chemical potential, we repeat these steps. Then, we find a region (or point), in (at) which the two order parameters, chiral and deconfinement, cross each other, i.e., equal each other. It is assumed that such a point represents phase transition(s) at the given chemical potential. In doing this, we get a set of points in a two-dimensional chart: the QCD phase diagram.

In Fig. 12, we compare five chiral phase diagrams, T/T_{c0} vs μ/μ_{c0}, with each other at $eB = 0.1$, 0.2, 0.3, 0.4, and 0.5 GeV^2 from top to bottom. T/T_{c0} are plotted against μ/μ_{c0}, where the two normalization quantities $T_{c0} = 0.15$ GeV and $\mu_{c0} = 0.3$ GeV were deduced from Ref. [38]. This should give an indication about the behavior of the critical temperature and the critical chemical potential of the system under the effect of the magnetic field. We conclude that both critical
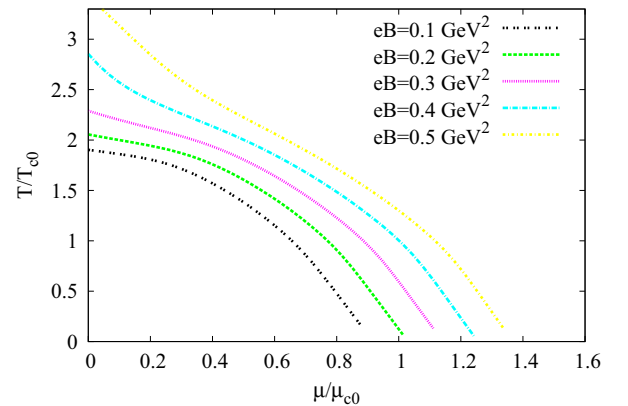

FIG. 12. (Color online) The chiral phase diagram, T/T_{c0} vs μ/μ_{c0}, at different values of the magnetic fields, $eB = 0.1$, 0.2, 0.3, 0.4, and 0.5 GeV^2 from top to bottom. The normalization quantities $T_{c0} = 0.15$ MeV and $\mu_{c0} = 0.3$ GeV were deduced in Ref. [38].
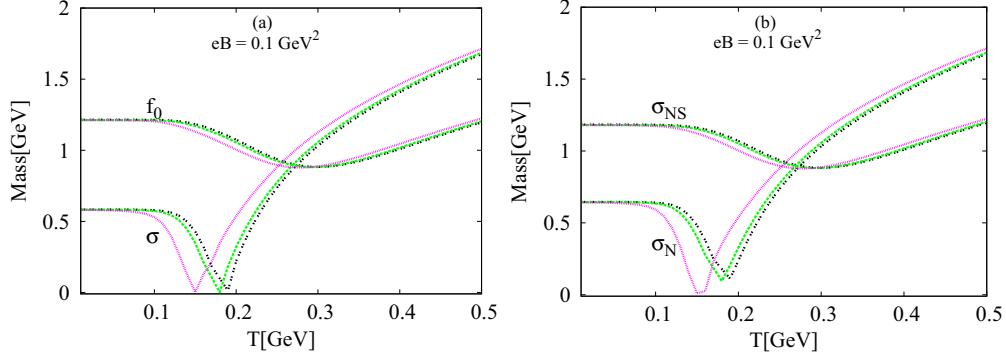
FIG. 13. (Color online) Left-hand panel (a): the scalar meson masses, m_σ from Eq. (16), m_{f_0} from Eq. (17), are given as functions of temperature at a constant magnetic field $eB = 0.1$ GeV^2 and different chemical potentials, $\mu = 0.0$ GeV (dotted curve), 0.1 GeV (dashed curve). and 0.2 GeV (double-dotted curve). Right-hand panel (b): the same as in the left-hand panel (a) but for $m_{\sigma_{NS}}$ from Eq. (18) and m_{σ_S} from Eq. (19).

temperature and critical chemical potential apparently increase with increasing magnetic field.

E. Meson masses

The masses can be deduced from the second derivative of the grand potential, Eq. (7) with respect to the corresponding fields, evaluated at its minimum, which is estimated at vanishing expectation values of all scalar and pseudoscalar fields

$$m_{i,ab}^2 = \left.\frac{\partial^2 \Omega(T,\mu_f)}{\partial \xi_{i,a} \partial \xi_{i,b}}\right|_{min}, \qquad (15)$$

where a and b range over $0, \ldots, 8$ and $\xi_{i,a}$ and $\xi_{i,b}$ are scalar and pseudoscalar mesonic fields, respectively. Obviously, i stands for scalar and pseudoscalar mesons.

The scalar meson masses are [66]

$$m_\sigma^2 = m_{s,00}^2 \cos^2 \theta_s + m_{s,88}^2 \sin^2 \theta_s + 2m_{s,08}^2 \sin \theta_s \cos \theta_s, \qquad (16)$$

$$m_{f_0}^2 = m_{s,00}^2 \sin^2 \theta_s + m_{s,88}^2 \cos^2 \theta_s - 2m_{s,08}^2 \sin \theta_s \cos \theta_s, \qquad (17)$$

$$m_{\sigma_{NS}}^2 = \tfrac{1}{3}\left(2m_{s,00}^2 + m_{s,88}^2 + 2\sqrt{2}m_{s,08}^2\right), \qquad (18)$$

$$m_{\sigma_S}^2 = \tfrac{1}{3}\left(m_{s,00}^2 + 2m_{s,88}^2 - 2\sqrt{2}m_{s,08}^2\right), \qquad (19)$$

where θ_s is the scalar mixing angle [66]

$$\theta_s = \frac{1}{2} \arctan\left[\frac{2(m_s^2)_{08}}{(m_s^2)_{00} - (m_s^2)_{88}}\right],$$

with $(m_s^2)_{ab} = m^2 \delta_{ab} - 6\mathcal{G}_{abc}\bar{\sigma}_c + 4\mathcal{F}_{abcd} \bar{\sigma}_c \bar{\sigma}_d$. The expressions for $\mathcal{G}_{abc}$ and $\mathcal{F}_{abcd}$ can be found in Ref. [66]. On the tree level, $\bar{\sigma}_c$ can be determined according to $\partial U(\bar{\sigma})/\partial \bar{\sigma}_a = 0 = m^2 \bar{\sigma}_a - 3\mathcal{G}_{abc}\bar{\sigma}_b \bar{\sigma}_c + (4/3)\mathcal{F}_{abcd} \bar{\sigma}_b \bar{\sigma}_c \bar{\sigma}_d - h_a$.

In Fig. 13, the scalar meson masses, m_σ from Eq. (16), and m_{f_0} from Eq. (17), are given as functions of temperature at a constant magnetic field $eB = 0.1$ GeV^2 and different chemical potentials $\mu = 0.0$ GeV (dotted curve), 0.1 GeV (dashed curve), and 0.2 GeV (double-dotted curve). We conclude that the scalar meson masses decrease as the temperature increases. This remains until T reaches the critical value. Then, the

vacuum effect becomes dominant and rapidly increases with the temperature. The effect of the chemical potential is very obvious. The masses decrease with the increase in chemical potential. This explains the phase diagram of temperatures and chemical potentials at a certain magnetic field. The decrease of the critical temperature with increasing chemical potential is represented by the low points (minima) in the thermal behavior of meson masses before switching on the vacuum effect.

In Fig. 14, the four scalar meson masses, m_σ from Eq. (16), m_{f_0} from Eq. (17), $m_{\sigma_{NS}}$ from Eq. (18), and m_{σ_S} from Eq. (19), are given as function of temperature at two values of chemical potential, $\mu = 0.1$ GeV in the left-hand panel (a) and $\mu = 0.2$ GeV in the right-hand panel (b), and different magnetic fields, $eB = 0.1, 0.2, 0.3, 0.4, 0.5$, and 0.6 GeV^2 from top to bottom. We notice that the scalar meson masses decrease as the temperature increases, until it reaches the critical temperature. Then, the vacuum effect gets dominant and apparently increases with the temperature. The effect of the magnetic field is very obvious. The masses increase as the magnetic field increases. This explains the phase diagram of temperatures and magnetic field at a certain chemical potential.

In Fig. 15, the normalized scalar meson masses, m_σ from Eq. (16), m_{f_0} from Eq. (17), $m_{\sigma_{NS}}$ from Eq. (18), and m_{σ_S} from Eq. (19) are given as functions of temperature at two values of chemical potential, $\mu = 0.1$ GeV in the left-hand panel (a) and $\mu = 0.2$ GeV in the right-hand panel (b), and different magnetic fields, $eB = 0.1, 0.2, 0.3, 0.4, 0.5$, and 0.6 GeV^2 from top to bottom. The normalization is done due to the lowest Matsubara frequencies, $2\pi T$; see Appendix C. At high temperatures, we notice that the masses of almost all meson states become temperature independent, i.e., they construct a kind of a universal bundle. This would be seen as a signature for meson dissociation into quarks. In other words, the meson states undergo a deconfinement phase transition. It is worthwhile to highlight that the various meson states likely have different critical temperatures.

At low temperatures, the scalar meson masses normalized to the lowest Matsubara frequency rapidly decrease as the temperature increases. Then, starting from the critical temperature, we find that the thermal dependence almost vanishes. The magnetic field effect is clear, namely the meson masses
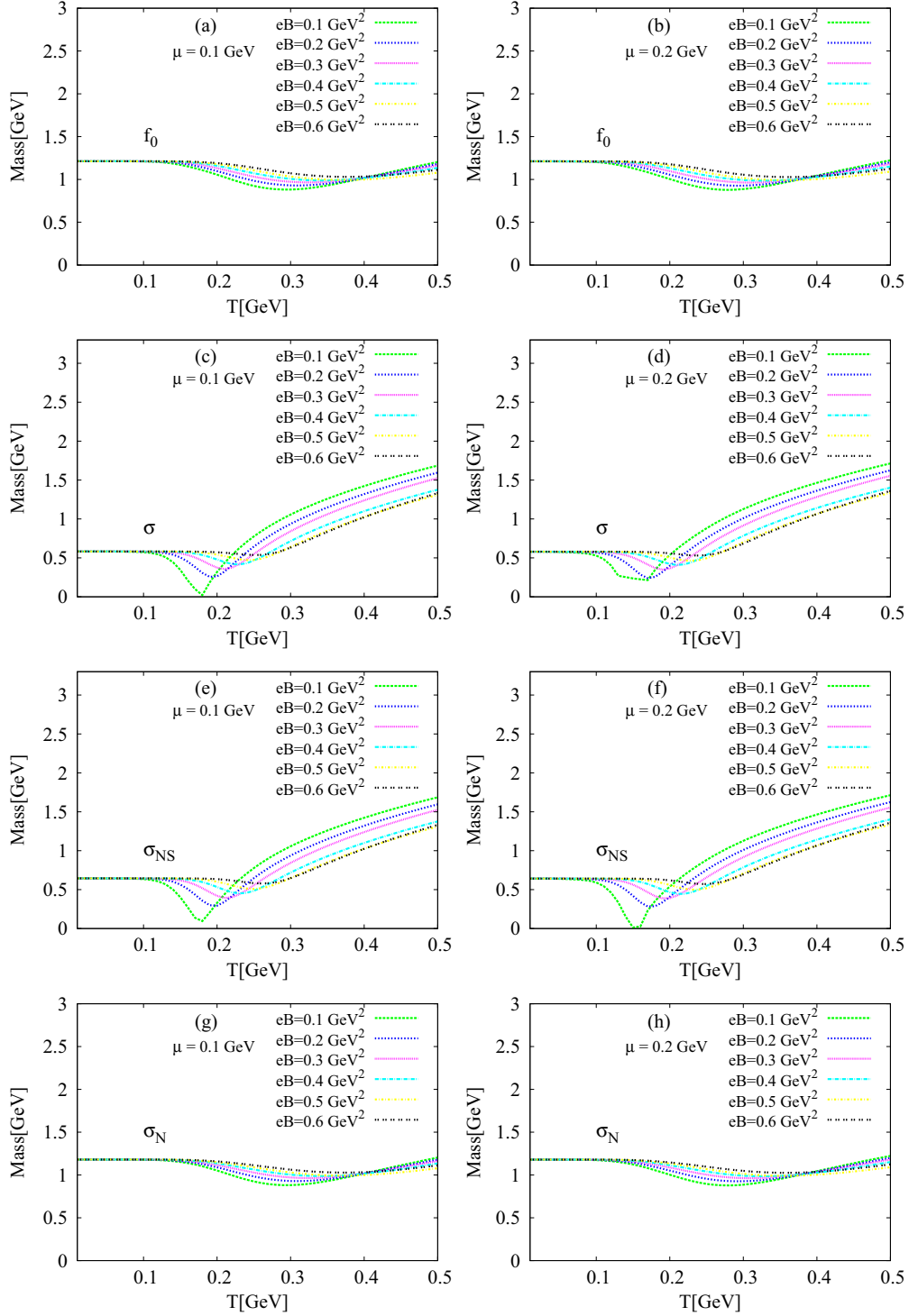
FIG. 14. (Color online) Left-hand panel (a): the four scalar meson masses are given as function of temperature at a constant chemical potential $\mu = 0.1$ GeV and different magnetic fields, $eB = 0.1$, 0.2, 0.3, 0.4, 0.5, and 0.6 GeV^2 from top to bottom. Right-hand panel (b): the same as in the left-hand panel but at chemical potential $\mu = 0.2$ GeV.

increase with increasing magnetic field. This characterizes the T vs eB phase diagram.

The pseudoscalar meson masses are [66]

$$m_{\eta'}^2 = m_{p,00}^2 \cos^2 \theta_p + m_{p,88}^2 \sin^2 \theta_p + 2m_{p,08}^2 \sin \theta_p \cos \theta_p, \tag{20}$$

$$m_{\eta}^2 = m_{p,00}^2 \sin^2 \theta_p + m_{p,88}^2 \cos^2 \theta_p - 2m_{p,08}^2 \sin \theta_p \cos \theta_p, \tag{21}$$

$$m_{\eta_{NS}}^2 = \tfrac{1}{3}\left(2m_{p,00}^2 + m_{p,88}^2 + 2\sqrt{2}m_{p,08}^2\right), \tag{22}$$

$$m_{\eta_S}^2 = \tfrac{1}{3}\left(m_{p,00}^2 + 2m_{p,88}^2 - 2\sqrt{2}m_{p,08}^2\right), \tag{23}$$
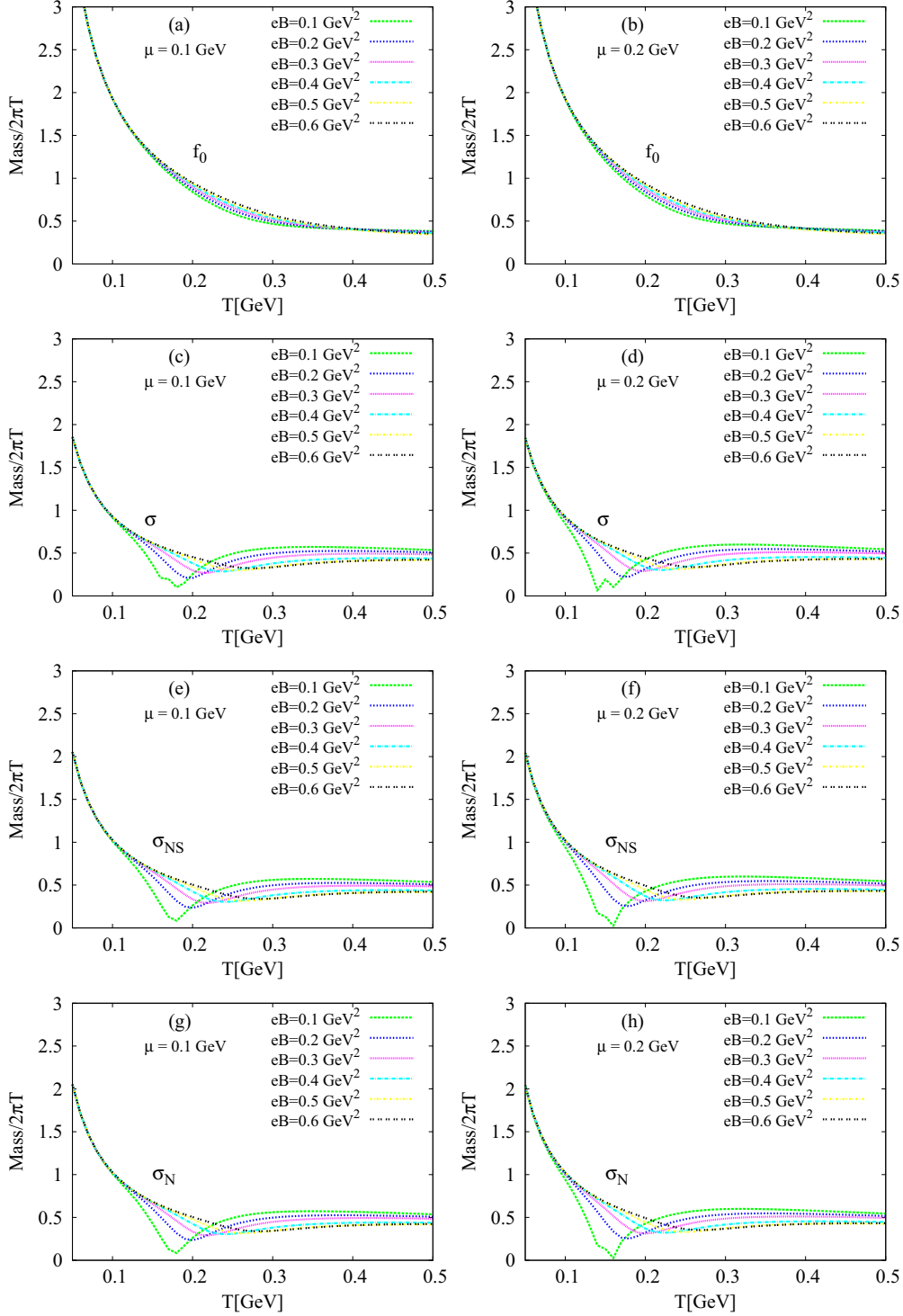
FIG. 15. (Color online) Left-hand panels: the scalar meson masses normalized with respect to the lowest Matsubara frequency are given as functions of temperature at a constant chemical potential $\mu = 0.1$ GeV and different magnetic fields, $eB = 0.1, 0.2, 0.3, 0.4, 0.5$ and 0.6 GeV^2 from top to bottom. Right-hand panels: the same as in the left-hand panels but at chemical potential $\mu = 0.2$ GeV.

where θ_p is the pseudoscalar mixing angle [66]

$$\theta_p = \frac{1}{2} \arctan \left[\frac{2(m_p^2)_{08}}{(m_p^2)_{00} - (m_p^2)_{88}} \right],$$

with $(m_p^2)_{ab} = m^2 \delta_{ab} + 6\mathcal{G}_{abc}\bar{\sigma}_c + 4\mathcal{H}_{abcd}\bar{\sigma}_c\bar{\sigma}_d$. The expressions for $\mathcal{H}_{abcd}$ are given in Eq. (11c) in Ref. [66].

In Fig. 16, the pseudoscalar meson masses, $m_{\eta'}$ from Eq. (20), m_η from Eq. (21), $m_{\eta_{NS}}$ from Eq. (22), and m_{η_S} from Eq. (23), are given as functions of temperature at a
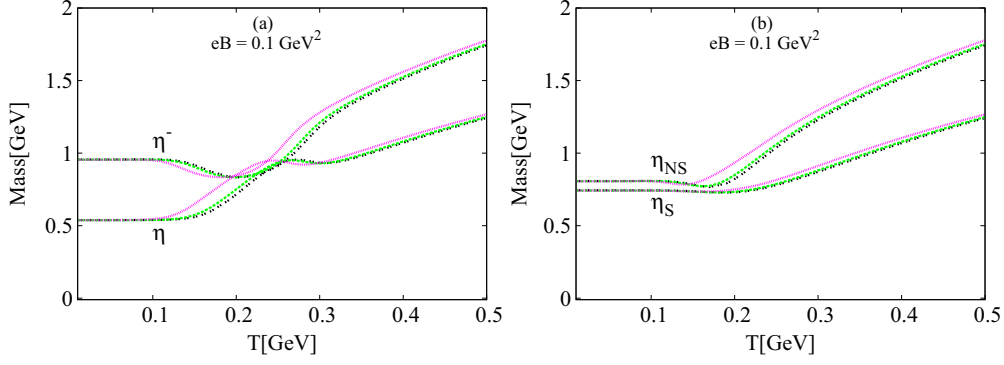
FIG. 16. (Color online) The same as in Fig. 13 but for pseudoscalar meson masses, $m_{\eta'}$ from Eq. (20), m_η from Eq. (21), $m_{\eta_{NS}}$ from Eq. (22), and m_{η_S} from Eq. (23).

constant magnetic field $eB = 0.1$ GeV^2 and different chemical potentials, $\mu = 0.0$ GeV (dotted curve), 0.1 GeV (dashed curve), and 0.2 GeV (double-dotted curve). It is obvious that the pseudoscalar meson masses remain constant at low temperature. At temperatures $\geqslant T_c$, the vacuum effect becomes dominant. Accordingly. the pseudoscalar meson masses increase with the temperature. We shall notice that even the contribution by the vacuum will be moderated through the normalization with respect to the lowest Matsubara frequency.

In Fig. 17, the four pseudoscalar meson masses, $m_{\eta'}$ from Eq. (20), m_η from Eq. (21), $m_{\eta_{NS}}$ from Eq. (22), and m_{η_S} from Eq. (23), are given as functions of temperature at two constant chemical potentials, $\mu = 0.1$ GeV in the left-hand panel (a) and $\mu = 0.2$ GeV in the right-hand panel (b), and different magnetic fields, $eB = 0.1, 0.2, 0.3, 0.4, 0.5,$ and 0.6 GeV^2 from top to bottom. Again, at low temperature, the masses remain temperature independent. At $T \geqslant T_c$, the vacuum effect is switched on. Accordingly, the masses increase rapidly with the temperature.

In Fig. 18, the four pseudoscalar meson masses, $m_{\eta'}$ from Eq. (20), m_η from Eq. (21), $m_{\eta_{NS}}$ from Eq. (22), and m_{η_S} from Eq. (23), normalized with respect to the lowest Matsubara frequency are given as functions of temperature at two constant chemical potentials, $\mu = 0.1$ GeV in the left-hand panel (a) and $\mu = 0.2$ GeV in the right-hand panel (b), and different magnetic fields, $eB = 0.1, 0.2, 0.3, 0.4,$ 0.5, and 0.6 GeV^2 from top to bottom. The normalization should result in temperature-independent mesonic states. This would be seen as a signature for meson dissociation into quarks. It is obvious that various critical temperatures can be assigned to various pseudoscalar meson states. The normalized masses start with high values reflecting confinement, especially at low temperatures. Then, they decrease as the temperature increases until the critical temperature, T_c, which differs for different meson states. At higher temperatures, the dependence of meson masses on temperature is almost entirely removed.

As introduced in Ref. [67], Table I presents a comparison between pseudoscalar meson nonets in various effective models, such as PLSM (present work) and PNJL [68], compared to the particle data group [69] and lattice QCD calculations [70,71]. The comparison for scalar states would be only partly possible. Some remarks are now in order. The

errors are deduced from the fitting for the parameters used in calculating the equations of state and other thermodynamic quantities. The output results are very precise for some of the lightest hadron resonances described by the present model, PLSM. An extended comparison is given in Ref. [67].

IV. CONCLUSIONS AND OUTLOOK

The QCD phase diagram at vanishing chemical potential and finite temperature subject to an external magnetic field gained prominence among high-energy physicists; for instance, our previous work [63] was based on two concepts in order to explain the effects of external magnetic field on the QCD phase diagram. Another study was done in the framework of the Nambu–Jona-Lasinio (NJL) model and Polyakov NJL (PNJL) model [73]. The main idea is that the scalar coupling parameter is taken to be dependent on the magnetic field intensity. Thus, the scalar coupling parameter decreases as the magnetic field increases. We also implemented the relation between the magnetic field and the scalar coupling parameter in order to fit the lattice QCD results [31]. We conclude the increase in the magnetic field increases the critical temperature.

In the presence work, we use the Polyakov linear-σ model and assume that the external magnetic field adds some restrictions to the quarks due to the existence of free charges in the plasma phase. In doing this, we apply Landau theory (Landau quantization), which quantizes of the cyclotron orbits of charged particles in a magnetic field. First, we have calculated and then analyzed the thermal evolution of the chiral condensates and the deconfinement order parameters. We notice that the Landau quantization requires additional temperature to drive the system through the chiral phase transition. Accordingly, we find that the values of the chiral condensates increase with increasing external magnetic field. In contrast to various previous studies, the effects of the external magnetic field are analyzed, systematically. Accordingly, the dependence of the critical temperatures of chiral and confinement phase transitions on the magnetic field could be characterized. We deduced T-μ curves using SU(3) PLSM in an external magnetic field.

Furthermore, by using the mean field approximation, we constructed the partition functions and then drove various
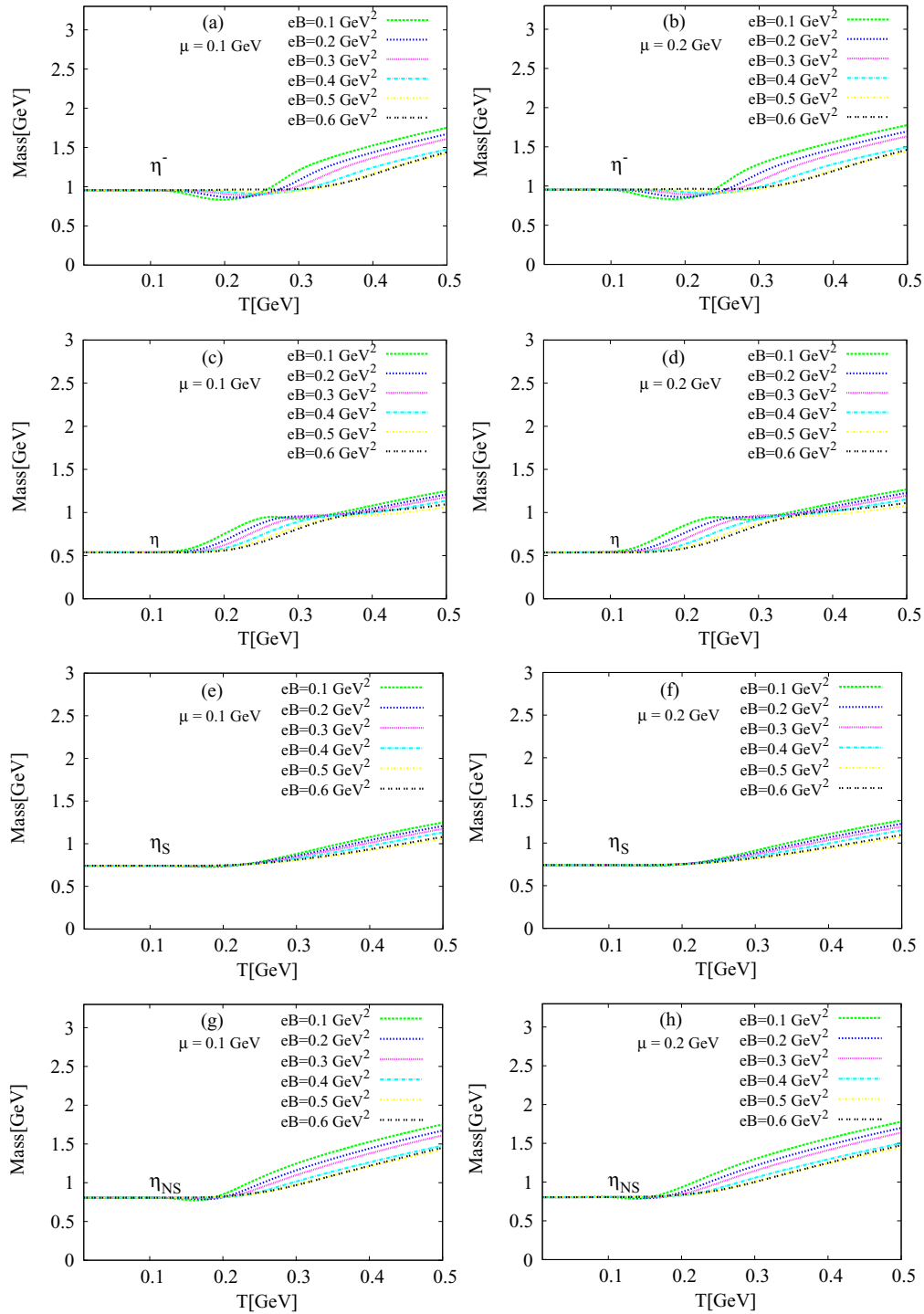
FIG. 17. (Color online) Left-hand panels: the pseudoscalar meson masses are given as functions of temperature at a constant chemical potential $\mu = 0.1$ GeV and different magnetic fields, $eB = 0.1, 0.2, 0.3, 0.4, 0.5,$ and 0.6 GeV^2 from top to bottom. The right-hand panels show the same as in the left-hand panels but at a constant chemical potential $\mu = 0.2$ GeV.

thermodynamic quantities, such as energy density and interaction rate (trace anomaly). Their dependence on temperature and chemical potential highlights that the effects of an external magnetic field on the chemical potential were disregarded in all calculations at finite chemical potential.

We have analyzed the first four non-normalized higher-order moments of particle multiplicity. The thermal evolution was studied at a constant chemical potential but different magnetic fields and also at a constant magnetic field but different chemical potentials. Doing this, the chiral phase diagram can be mapped out. We determined the irregular behavior as a function of T and μ. We found that increasing temperature rapidly increases the four moments, and the thermal dependence is obviously enhanced when moving
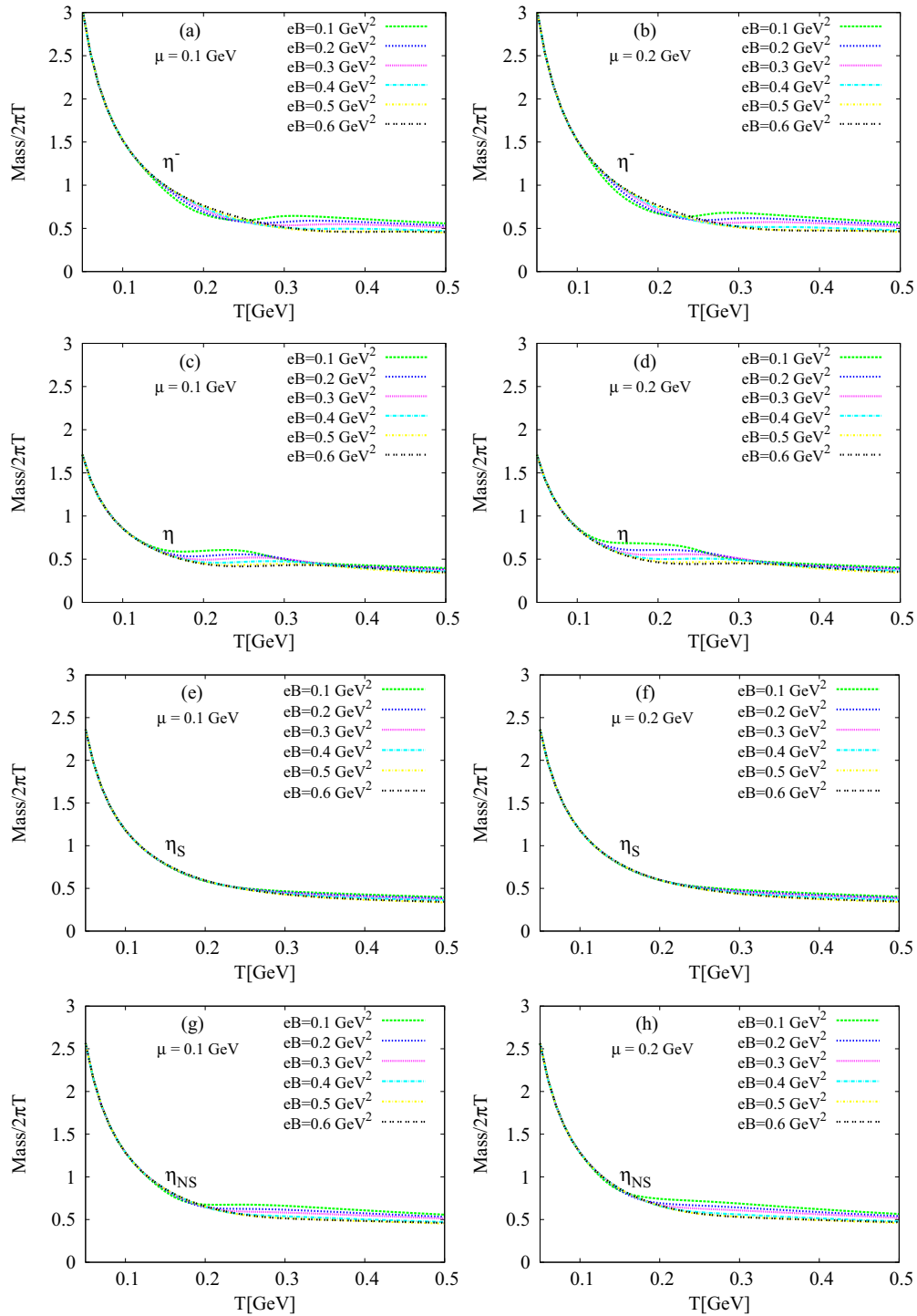
FIG. 18. (Color online) Left-hand panels: the pseudoscalar meson masses normalized to the lowest Matsubara frequency are given as functions of temperature at a constant chemical potential $\mu = 0.1$ GeV and different magnetic fields, $eB = 0.1, 0.2, 0.3, 0.4, 0.5$, and 0.6 GeV^2 from top to bottom. The right-hand panels show the same as in the left-hand panel but at a constant chemical potential $\mu = 0.2$ GeV.

from lower to higher orders. The values of the moment are increasing as we increase the chemical potential. But the critical temperature T_c decreases with μ. The peaks are positioned at the critical temperature.

The higher-order moments normalized to temperature are studied at a constant chemical potential and different magnetic

fields. Also, they are studied at different chemical potentials and a constant magnetic field. The statistical normalization requires scaling with respect to the standard deviation σ, where σ is related to the susceptibility χ or the fluctuations. Due to the sophisticated derivations, the discussion was limited to dimensionless higher-order moments. This can be done when

TABLE I. A comparison between pseudoscalar meson masses, $J^{PC} = 0^{-+}$, in MeV and the corresponding results from PNJL [68]. Both are compared with the experimental measurements: the Particle Data Group (PDG) [69] and the lattice QCD calculations [70,71].

Symbol	PDG [69]	Present work	PNJL [68,72]	Lattice QCD	
				Hot QCD [70]	PACS-CS [71]
π	134.970 ± 6.9	120	126	134 ± 6	135.4 ± 6.2
K	497.614 ± 24.8	509	490	422.6 ± 11.3	498 ± 22
η	547.853 ± 27.4	553	505	579 ± 7.3	688 ± 32
η'	957.78 ± 60	965	949		

the normalization is done with respect to the temperature or chemical potential. We find that the higher-order moments increase with the magnetic field. We found that the moments increase with the chemical potentials, and that the peaks at corresponding critical temperatures can be used to map out the chiral phase diagrams: T vs eB and T vs μ.

The effects of the magnetic field on the chiral phase transition have been evaluated. There are different methods proposed to calculate the critical temperature and chemical potential, μ_c, through implementing fluctuations in the normalized higher-order moments or by the order parameters. The latter was implemented in the present work. It is obvious that PLSM has two types of order parameter. The first one gives the chiral phase transition and is related to strange and nonstrange chiral condensates. The second one gives hints for the deconfinement phase transition. Therefore, we can follow the principle that, at a constant magnetic field and by using strange and nonstrange chiral condensates, a dimensionless quantity would reflect the difference between the nonstrange and strange condensates $\Delta_{q,s}(T)$ as a function of temperature at fixed chemical potentials; i.e., a chiral phase transition. At the same chemical potential, we can deduce the other order parameter related to the Polyakov-loop fields as a function of temperature. Both calculations give one point at which the two order parameters cross each other. It is assumed that such a point represents the transition point at the given chemical potential. We repeat this at various chemical potentials and get a set of points in a two-dimensional chart: the QCD phase diagram. We have compared five QCD phase diagrams, T/T_{c0} vs μ/μ_{c0}, with each other at five different values of the magnetic field. We found that both critical temperature and critical chemical potential increase with increasing magnetic field.

The masses can be deduced from the second derivative of the grand potential with respect to the corresponding fields, evaluated at its minimum, which is estimated at vanishing expectation values of all scalar and pseudoscalar fields. We have studied scalar and pseudoscalar meson masses as functions of temperature at two different values of magnetic field and different chemical potentials. We concluded that the meson masses decrease as the temperature increases. This continues until T reaches the critical value. Then, the vacuum effect becomes dominant and rapidly increases with the temperature. The decrease of the critical temperature with increasing chemical potential is represented by the low points (minima) in the thermal behavior of meson masses before switching on the vacuum effect. At low temperatures, the scalar meson

masses normalized to the lowest Matsubara frequency rapidly decrease as the temperature increases. Then, starting from the critical temperature, we find that the thermal dependence almost vanishes. Furthermore, the meson masses increase with increasing magnetic field. This characterizes the T vs eB phase diagram. At high temperatures, we notice that the masses of almost all meson states become temperature independent, i.e., constructing kind of a universal line. This would be seen as a signature for meson dissociation into quarks. In other words, the meson states undergo a deconfinement phase transition. It is worthwhile to highlight that the various meson states likely have different critical temperatures.

APPENDIX A: MAGNETIC CATALYSIS

For simplicity, we assume that the direction of the magnetic field B goes along the z direction. From the magnetic catalysis [74] and by using Landau quantization, we find that when the system is affected by a strong magnetic field, the quark dispersion relation will be modified to be quantized by the Landau quantum number, $n \geqslant 0$, and therefore the concept of dimensional reduction will be applied:

$$E_u = \sqrt{p_z^2 + m_q^2 + |q_u|(2n + 1 - \sigma)B}, \qquad (A1)$$

$$E_d = \sqrt{p_z^2 + m_q^2 + |q_d|(2n + 1 - \sigma)B}, \qquad (A2)$$

$$E_s = \sqrt{p_z^2 + m_s^2 + |q_s|(2n + 1 - \sigma)B}, \qquad (A3)$$

where σ is related to the spin quantum number and S ($\sigma = \pm S/2$). Here, we replace $2n + 1 - \sigma$ by one quantum number ν, where $\nu = 0$ is the lowest Landau level (LLL). The maximum Landau level (MLL) was determined according to Eq. (A7) [75]. The masses m_f, where f runs over u-, d-, and s-quark masses,

$$m_q = g \frac{\sigma_x}{2}, \qquad (A4)$$

$$m_s = g \frac{\sigma_y}{\sqrt{2}}. \qquad (A5)$$

We apply another magnetic catalysis property [74], namely the dimensional reduction. As the name says, the dimensions will be reduced as $D \longrightarrow D - 2$. In this situation, the three-momentum integral will transformed into a one-momentum integral,

$$T \int \frac{d^3 p}{(2\pi)^3} \longrightarrow \frac{|q_f| BT}{2\pi} \sum_{\nu=0}^{\infty} \int \frac{dp}{2\pi}(2 - 1\delta_{0\nu}), \quad \text{(A6)}$$

where $2 - 1\delta_{0\nu}$ represents the degeneracy in the Landau level, since for the LLL we have single degeneracy and doublets for the upper Landau levels,

$$\nu_{\max} = \frac{\Lambda_{QCD}^2}{2|q_f| B}. \quad \text{(A7)}$$

We use m_q and m_s for non-strange and strange quark masses, i.e., the masses of light quarks degenerate. This is not the case for the electric charges. In Sec. II, q_u, q_d, and q_s are described.

APPENDIX B: MINIMIZATION CONDITION

We notice that the thermodynamic potential density as given in Eq. (7), which has seven parameters m^2, h_x, h_y, λ_1, λ_2, c, and g, two unknown condensates σ_x and σ_y, and the order parameters for the deconfinement, ϕ and ϕ^*. The six parameters $m^2, h_x, h_y, \lambda_1, \lambda_2$, and c are fixed in the vacuum by six experimentally known quantities [55]. In order to evaluate the unknown parameters σ_x, σ_y, ϕ, and ϕ^*, we minimize the thermodynamic potential, Eq. (7), with respect to σ_x, σ_y, and ϕ and ϕ^* or ϕ_R and ϕ_R^*. Doing this, we obtain a set of four equations of motion,

$$\frac{\partial \Omega_1}{\partial \sigma_x} = \frac{\partial \Omega_1}{\partial \sigma_y} = \frac{\partial \Omega_1}{\partial \phi} = \frac{\partial \Omega_1}{\partial \phi^*}\bigg|_{min} = 0, \quad \text{(B1)}$$

meaning that $\sigma_x = \bar{\sigma}_x$, $\sigma_y = \bar{\sigma}_y$, $\phi = \bar{\phi}$ and $\phi^* = \bar{\phi}^*$ are the global minimum.

APPENDIX C: MATSUBARA FREQUENCIES

In finite-temperature field theory, the Matsubara frequencies are a summation over the discrete imaginary frequency, $S_\eta = T \sum_{i\omega_n} g(i\omega_n)$, where $g(i\omega_n)$ is a rational function,

$\omega_n = 2n\pi T$ for bosons and $\omega_n = (2n+1)\pi T$ for fermions and $n = 0, \pm 1, \pm 2, \dots$ is an integer playing the role of a quantum number. By using Matsubara weighting function $h_\eta(z)$, which has simple poles exactly located at $z = i\omega_n$, then

$$S_\eta = \frac{T}{2\pi i} \oint g(z) h_\eta(z) dz, \quad \text{(C1)}$$

where $\eta = \pm$ stands for the statistic sign for bosons and fermions, respectively. $h_\eta(z)$ can be chosen depending on which half plane the convergence is to be controlled,

$$h_\eta(z) = \begin{cases} \eta \dfrac{1 + n_\eta(z)}{T}, \\ \eta \dfrac{n_\eta(z)}{T}, \end{cases} \quad \text{(C2)}$$

where $n_\eta(z) = \left(1 + \eta e^{z/T}\right)^{-1}$ is the single-particle distribution function.

The mesonic masses are conjectured to have contributions from Matsubara frequencies [76]. Furthermore, at high temperatures, $\geqslant T_c$, the behavior of the thermodynamic quantities, including the quark susceptibilities and the masses are affected by the interplay between the lowest Matsubara frequency and the Polyakov-loop correction [77]. We apply normalization for the different mesonic sectors with respect to the lowest Matsubara frequency [78] in order to characterize the dissolving temperature of the mesonic bound states. It is found that the different mesonic states have different dissolving temperatures. This would mean that the different mesonic states have different T_c's at which the bound mesons begin to dissolve into quarks. Therefore, the normalized masses should not be different at $T > T_c$. To a large extent, their thermal and density dependence should be removed, so that the remaining effects are defined by the free energy [76], i.e., the masses of *free* besons are defined by m_l.

That the masses of almost all mesonic states become independent on T, i.e., constructing a kind of a universal line, is seen as a signature for meson dissociation into quarks. It is a deconfinement phase transition, where the quarks behave almost freely. In other words, the characteristic temperature should not be universal, as well. So far, we conclude that the universal T_c characterizing the QCD phase boundary is indeed an approximative average (over various bound states).

[1] D. R. Rischke, Prog. Part. Nucl. Phys. **52**, 197 (2004).
[2] R. Gatto and M. Ruggieri, Phys. Rev. D **82**, 054027 (2010).
[3] M. Ruggieri, PoS(FACES QCD)019 (2010).
[4] R. Gatto and M. Ruggieri, Phys. Rev. D **83**, 034016 (2011).
[5] E. S. Fraga, B. W. Mintz, and J. Schaffner-Bielich, Phys. Lett. B **731**, 154 (2014).
[6] J. O. Andersen, W. R. Naylor, and A. Tranberg, J. High Energy Phys. 04 (2014) 187.
[7] V. Skokov, Phys. Rev. D **85**, 034026 (2012).
[8] C. Bonati, M. D'Elia, M. Mariti, F. Negro, and F. Sanfilippo, Phys. Rev. Lett. **111**, 182001 (2013).
[9] M. D'Elia, S. Mukherjee, and F. Sanfilippo, Phys. Rev. D **82**, 051501 (2010).
[10] G. Endrdi, J. High Energy Phys. 04 (2013) 023.
[11] S. P. Klevansky and R. H. Lemmer, Phys. Rev. D **39**, 3478 (1989).
[12] V. P. Gusynin, V. A. Miransky, and I. A. Shovkovy, Phys. Lett. B **349**, 477 (1995).
[13] A. Y. Babansky, E. V. Gorbar, and G. V. Shchepanyuk, Phys. Lett. B **419**, 272 (1998).
[14] K. G. Klimenko, in *Proceedings of the 5th International Workshop On Thermal Field Theories and Their Applications*, edited by U. Heinz (Regensburg University, Regensburg, Germany, 1999).
[15] G. W. Semenoff, I. A. Shovkovy, and L. C. R. Wijewardhana, Phys. Rev. D **60**, 105024 (1999).

[16] A. Goyal and M. Dahiya, Phys. Rev. D **62**, 025022 (2000).

[17] B. Hiller, A. A. Osipov, A. H. Blin, and J. da Providéncia, SIGMA Bull. **4**, 024 (2008).

[18] A. Ayala, A. Bashir, A. Raya, and E. Rojas, Phys. Rev. D **73**, 105009 (2006).

[19] J. K. Boomsma and D. Boer, Phys. Rev. D **81**, 074005 (2010).

[20] S. P. Klevansky, Rev. Mod. Phys. **64**, 649 (1992).

[21] D. P. Menezes, M. B. Pinto, S. S. Avancini, A. P. Martinez, and C. Providencia, Phys. Rev. C **79**, 035807 (2009).

[22] D. P. Menezes, M. Benghi Pinto, S. S. Avancini, and C. Providencia, Phys. Rev. C **80**, 065805 (2009).

[23] I. A. Shushpanov and A. V. Smilga, Phys. Lett. B **402**, 351 (1997).

[24] N. O. Agasian and I. A. Shushpanov, Phys. Lett. B **472**, 143 (2000).

[25] T. D. Cohen, D. A. McGady, and E. S. Werbos, Phys. Rev. C **76**, 055201 (2007).

[26] D. Kabat, K. M. Lee, and E. Weinberg, Phys. Rev. D **66**, 014004 (2002).

[27] V. A. Miransky and I. A. Shovkovy, Phys. Rev. D **66**, 045006 (2002).

[28] K. G. Klimenko and V. C. Zhukovsky, Phys. Lett. B **665**, 352 (2008).

[29] K. Fukushima, M. Ruggieri, and R. Gatto, Phys. Rev. D **81**, 114031 (2010).

[30] V. V. Braguta, P. V. Buividovich, M. N. Chernodub, and M. I. Polikarpov, Phys. Lett. B **718**, 667 (2012).

[31] G. S. Bali, F. Bruckmann, G. Endrodi, Z. Fodor, S. D. Katz, S. Krieg, A. Schafer, and K. K. Szabo, J. High Energy Phys. 02 (2012) 044.

[32] G. S. Bali, F. Bruckmann, G. Endrodi, Z. Fodor, S. D. Katz, and A. Schafer, Phys. Rev. D **86**, 071502 (2012).

[33] P. V. Buividovich, M. N. Chernodub, E. V. Luschevskaya, and M. I. Polikarpov, Phys. Lett. B **682**, 484 (2010).

[34] A. J. Mizher, M. N. Chernodub, and E. S. Fraga, Phys. Rev. D **82**, 105016 (2010).

[35] M. Ruggieri, M. Tachibana, and V. Greco, J. High Energy Phys. 07 (2013) 165.

[36] L. D. Landau and E. M. Lifshitz, *Quantum Mechanics* (Butterworth Heinemann, Amesterdam, 1965).

[37] G. N. Ferrari, A. F. Garcia, and M. B. Pinto, Phys. Rev. D **86**, 096005 (2012).

[38] A. Tawfik, N. Magdy, and A. Diab, Phys. Rev. C **89**, 055210 (2014).

[39] M. Gell-Mann and M. Levy, Nuovo Cimento. **16**, 705 (1960).

[40] J. T. Lenaghan and D. H. Rischke, J. Phys. G **26**, 431 (2000).

[41] N. Petropoulos, J. Phys. G **25**, 2225 (1999).

[42] M. Levy, Nuovo Cimento **52**, 23 (1967).

[43] B. Hu, Phys. Rev. D **9**, 1825 (1974).

[44] J. Schechter and M. Singer, Phys. Rev. D **12**, 2781 (1975).

[45] H. B. Geddes, Phys. Rev. D **21**, 278 (1980).

[46] A. M. Polyakov, Phys. Lett. B **72**, 477 (1978).

[47] L. Susskind, Phys. Rev. D **20**, 2610 (1979).

[48] B. Svetitsky and L. G. Yaffe, Nucl. Phys. B **210**, 423 (1982).

[49] B. Svetitsky, Phys. Rep. **132**, 1 (1986).

[50] J. Wambach, B.-J. Schaefer, and M. Wagner, Acta Phys. Pol. Suppl. **3**, 691 (2010).

[51] T. Kahara and K. Tuominen, Phys. Rev. D **78**, 034015 (2008).

[52] B.-J. Schaefer and M. Wagner, Prog. Part. Nucl. Phys. **62**, 381 (2009).

[53] H. Mao, J. Jin, and M. Huang, J. Phys. G **37**, 035001 (2010).

[54] J. T. Lenaghan, D. H. Rischke, and J. Schaffner-Bielich, Phys. Rev. D **62**, 085008 (2000).

[55] B. J. Schaefer and M. Wagner, Phys. Rev. D **79**, 014018 (2009).

[56] O. Scavenius, A. Mocsy, I. N. Mishustin, and D. H. Rischke, Phys. Rev. C **64**, 045202 (2001).

[57] K. Fukushima, Phys. Lett. B **591**, 277 (2004).

[58] S. Rossner, C. Ratti, and W. Weise, Phys. Rev. D **75**, 034007 (2007).

[59] C. Ratti, M. A. Thaler, and W. Weise, Phys. Rev. D **73**, 014019 (2006).

[60] K. Fukushima, Phys. Rev. D **77**, 114028 (2008).

[61] B.-J. Schaefer, J. M. Pawlowski, and J. Wambach, Phys. Rev. D **76**, 074023 (2007).

[62] Simon Hands, Timothy J. Hollowood, and Joyce C. Myers, J. High Energy Phys. 07 (2010) 086.

[63] A. N. Tawfik and N. Magdy, Phys. Rev. C **90**, 015204 (2014).

[64] A. Tawfik, Int. J. Mod. Phys. A **29**, 1430021 (2014).

[65] A. Tawfik, Adv. High Energy Phys. **2013**, 22 (2013).

[66] V. K. Tiwari, Phys. Rev. D **88**, 074017 (2013).

[67] A. N. Tawfik and A. M. Diab, Phys. Rev. C **91**, 015204 (2015).

[68] P. Costa, M. C. Ruivo, C. A. de Sousa, and Y. L. Kalinovsky, Phys. Rev. D **70**, 116013 (2004); **71**, 116002 (2005); P. Costa, M. C. Ruivo, C. A. de Sousa, H. Hansen, and W. M. Alberico, *ibid.* **79**, 116003 (2009).

[69] J. Beringer *et al.* (Particle Data Group), Phys. Rev. D **86**, 010001 (2012).

[70] A. Bazavov *et al.* (HotQCD Collaboration), Phys. Rev. D **85**, 054503 (2012).

[71] S. Aoki *et al.* (PACS-CS Collaboration), Phys. Rev. D **81**, 074503 (2010).

[72] T. Xia, L. He, and P. Zhuang, Phys. Rev. D **88**, 056013 (2013).

[73] M. Ferreira, P. Costa, O. Lourenco, T. Frederico, and C. Providencia, Phys. Rev. D **89**, 116011 (2014).

[74] I. A. Shovkovy, in *Strongly Interacting Matter in Magnetic Fields*, edited by D. Kharzeev, K. Landsteiner, A. Schmitt, and H.-U. Yee, *Lecture Notes in Physics* Vol. 871 (Springer, Berlin, 2013), p. 13.

[75] S. Ghosh, S. Mandal, and S. Chakrabarty, Phys. Rev. C **75**, 015805 (2007).

[76] W. Florkowski and B. L. Friman, Z. Phys. A **347**, 271 (1994).

[77] K. Dusling, C. Ratti, and I. Zahed, Phys. Rev. D **79**, 034027 (2009).

[78] A. Tawfik, Soryushiron Kenkyu **114**, B48 (2006).